Audevard, Jérémy, Navarro-Ruiz, Javier, Bernardin, Vincent, Tison, Yann, Corrias, Anna, Del Rosal, Iker, Favre-Réguillon, Alain, Philippe, Régis, Gerber, Iann C. and Serp, Philippe (2023) *Adjustment of the single atom/nanoparticle ratio in Pd/CNT catalysts for phenylacetylene selective hydrogenation.* ChemCatChem, 15 (11). ISSN 1867-3880.

ChemCatChem

The European Society Journal for Catalysis

Accepted Article

Title: Adjustment of the single atom/nanoparticle ratio in Pd/CNT catalysts for phenylacetylene selective hydrogenation

Authors: Jérémy Audevard, Javier Navarro-Ruiz, Vincent Bernardin, Yann Tison, Anna Corrias, Iker Del Rosal, Alain Favre-Réguillon, Régis Philippe, Iann C. Gerber, and Philippe Serp

Adjustment of the single atom/nanoparticle ratio in Pd/CNT catalysts for phenylacetylene selective hydrogenation

Jérémy Audevard,[a] Javier Navarro-Ruiz,[b] Vincent Bernardin,[c] Yann Tison,[d] Anna Corrias,[e] Iker Del Rosal,[b] Alain Favre-Réguillon,[c,f] Régis Philippe,[c] Iann C. Gerber,[b] and Philippe Serp[a,*]

[a] *LCC–CNRS, Université de Toulouse, UPR 8241 CNRS, INPT, Toulouse, France*

[b] *Université de Toulouse, INSA–CNRS–UPS, LPCNO, Toulouse F-31077, France*

[c] *Université Lyon, CP2M, UMR 5128 CNRS - CPE Lyon, 43 boulevard du 11 novembre 1918, F-69100 Villeurbanne, France.*

[d] *Université de Pau et des Pays de l'Adour, E2S UPPA, CNRS, IPREM, Pau, France*

[e] *School of Chemistry and Forensic Science, University of Kent Canterbury, Ingram Building, Room 118, CT2 7NH, UK*

[f] *Département Chimie-Vivant-Santé, Conservatoire National des Arts et Métiers, 292 rue Saint Martin, F-75003 Paris, France*

ABSTRACT: Pd/C catalysts are widely used for hydrogenation reactions in the chemical industry. One of the reasons for their high activity is the ability of Pd nanoparticles (Pd_{NP}) to dissociate H_2 and promote H-spillover. Nevertheless, for selective hydrogenation unpromoted Pd/C catalysts show disappointing results. The use of supported Pd single atom (Pd_{SA}) catalysts permits to achieve high selectivity. However, Pd_{SA} show low activity because they have difficulty in activating H_2. A cooperative catalysis between Pd_{NP} and Pd_{SA} operates for the hydrogenation of alkenes thanks to the H-spillover, which makes it possible to obtain active isolated Pd_{SA}-H species. Here, we present experimental and computational results obtained for phenylacetylene hydrogenation on Pd/CNT catalysts showing different Pd_{SA}/Pd_{NP} ratios. Tuning this ratio allows doubling the activity while reaching high selectivity to styrene at high conversion. DFT calculations suggest that the first coordination sphere of Pd_{SA} has a pronounced effect on their reactivity.

KEYWORDS: hydrogenation, nanoparticles, palladium, carbon, hydrogen

Introduction

Alkynes can be selectively reduced to their corresponding olefins on heterogeneous catalysts by clean and inexpensive H_2. Selectively hydrogenating C≡C to C=C is an industrial process used for the purification of alkene-containing hydrocarbon streams from alkyne compound impurities, which act as catalyst poison in the production of polymer-grade olefins.[1] The advantage of this process is that the unwanted alkynes are directly converted to the target olefins. Thus, removal of phenylacetylene (PhA), an impurity from styrene (ST) by selective hydrogenation, is a process of industrial importance because PhA poisons and deactivates polymerization catalysts in polystyrene production units. Thermodynamic and/or kinetic parameters, which depend on catalyst formulation, can influence selective hydrogenation.[2]

Supported Pd catalysts are very efficient hydrogenation catalysts because the activation energy for H_2 dissociative chemisorption on palladium surface is low,[3] and the diffusion of chemisorbed hydrogen is high.[4] It is also well-known that hydrogen not only adsorbs on the Pd surface but also absorbs on its subsurface (Pd hydride phases).[5] Pd-based catalysts are known for their high selectivity in alkyne hydrogenation, as long as the thermodynamic is oriented towards stronger adsorption of the alkyne on Pd relative to the alkene to prevent over-hydrogenation.[6] Different levers can be operated to improve the selectivity of the reaction on Pd such as: i) controlling the metal particle-size, ii) adding a second metal or specific additive (selective poisoning), iii) alloying (site-isolation), iv) confinement or v) changing the support, among others. [2, 7] Most of these strategies, like site-isolation or selective poisoning of active sites, lead to: i) a non-optimal metal utilization, since a large portion of Pd active sites are covered and inaccessible to reactants, and/or ii) toxic and environmentally unfriendly catalyst formulations. Consequently, the improvement of selectivity is often at the cost of activity.

An important factor in the effectiveness of the selective hydrogenation catalyst is the metal particle size. Indeed, both the electronic properties and relative ratio of various types of surface atoms on metal particles change appreciably when the number of atoms in an isolated metal particle is reduced. Therefore, a change in the Pd particle size could be expected to have an influence on the adsorption of PhA and ST because of electronic or geometric effects, and thus on their relative reaction rates. Nevertheless, reducing particle size in a Pd-supported catalyst can have other effects, such as on the charge transfer with the support[8] or on the nature of the PdH_x hydride phases,[9] which in turn can influence the interaction with the reactants. In fact, contradictory results on the influence of metal dispersion on catalytic performance have been reported for PhA selective hydrogenation.[10] Styrene selectivity has been reported to increase[10a, 10f] or to decrease[10b, 10c, 10e-g] when the Pd dispersion increases, or may not be affected by Pd dispersion.[10d] Different size ranges can be distinguished (Fig. 1a): large Pd nanoparticles (Pd_{NP}), small Pd particles, clusters and isolated palladium single atoms (Pd_{SA}). Although rationalizing the contradictory results from the literature is not easy because the different studies have used different supports, which can affect the charge transfer,[10d] as well as different operating conditions, some tendencies can be underlined. Very large Pd_{NP} (*zone I*, Fig. 1b) does not seem to be selective because of the presence of the

2

β-PdH phase, which increases with increasing the Pd_{NP} size, and is believed to contribute to alkyne over-hydrogenation.[10a, 10f]
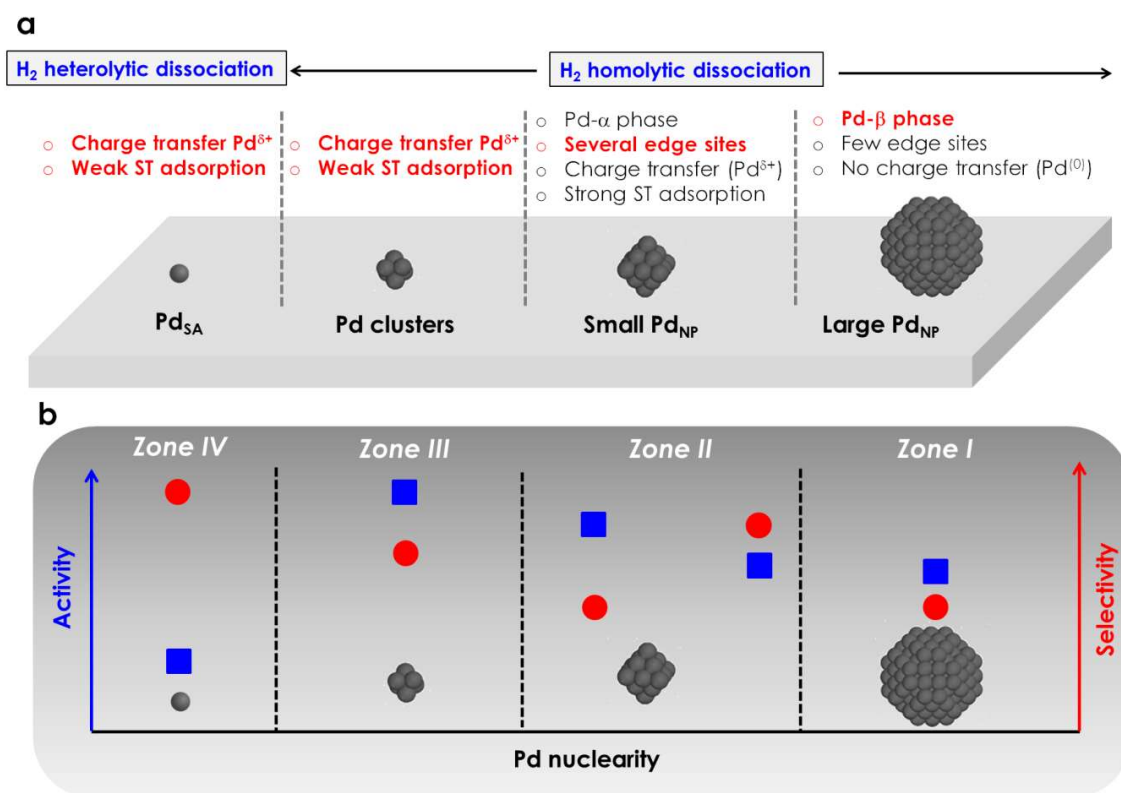
Figure 1. Influence of Pd dispersion on: (**a**) catalyst features; and (**b**) catalyst performance for PhA selective hydrogenation to ST.

This effect could counterbalance the geometric effect, *i.e.*, large Pd_{NP} contain fewer edge sites that are favorable for ST adsorption and further hydrogenation.[10g] For small Pd_{NP} (2-10 nm, *zone II*, Fig. 1b), it is often argued that it is the stronger adsorption energy of ST on small Pd_{NP} that induces a decrease in selectivity.[10b, 10e] This has been confirmed by DFT calculations, at least for Pd_{NP} with more than 30 atoms.[11] Interestingly, for Pd clusters with fewer than 30 Pd atoms, the ST adsorption weakens rapidly with a decrease in size due to a geometric effect. This could explain the high activity and selectivity reported when using highly dispersed Pd catalysts (*zone III*, Fig. 1b).[12] Finally, when using Pd_{SA} (*zone IV*, Fig. 1b), optimal site-isolation allows the weakest adsorption of ST and the possibility of reaching very high selectivity at high conversion.[13] However, in this latter case, the important energy barrier to achieve the activation of H_2 *via* heterolytic dissociation makes Pd_{SA} significantly less active than higher nuclearity Pd species, for which easy homolytic dissociation of H_2 occurs.[14] We recently demonstrated that this disadvantage of Pd_{SA} in hydrogenation catalysis could be overcome by mixing them with Pd_{NP} on the same carbon support.[15] Dihydrogen is readily activated on Pd_{NP} and H-spillover provided Pd_{SA}-H species, which are more active than Pd_{NP} for non-selective alkene hydrogenation.

3

Herein, we wanted to determine if the same concept could be applied to selective hydrogenation. Thus, Pd/CNT catalysts presenting different proportions of Pd_{SA} and Pd_{NP} for a given metal loading have been prepared, fully characterized, and tested for PhA selective hydrogenation both in batch and flow.

Results and discussion

This study involves preparing CNT-supported Pd catalysts presenting similar metal loading and containing mixtures of Pd_{SA} and Pd_{NP} in different proportions. The preparation and characterization of this type of catalyst are not easy. First, most carbon supports present in variable quantities sites capable of stabilizing Pd_{SA}.[16] Consequently, most carbon-supported Pd_{NP}-based catalysts (including commercial ones) contain Pd_{SA}, which can be easily visualized by aberration-corrected scanning transmission electron microscopy (AC-STEM).[17] On the other hand, the preparation and characterization of catalysts containing exclusively Pd_{SA} with significant metal loading (≥ 1% w/w) is difficult. In particular, the presence of clusters in such catalysts is not always easy to demonstrate, even by combining several techniques, such as high-angle annular dark-field STEM imaging (HAADF-STEM), EXAFS, and XPS (DRIFTS analysis of carbon surfaces coupled to a probe molecule proves to be very challenging).[18]

Preparation and characterization of Pd/CNT catalysts with different single atom/nanoparticle ratio

Four different Pd/CNT catalysts with a nominal Pd loading of 1.2% w/w have been prepared, in which the Pd_{SA}/Pd_{NP} ratio (a numerical ratio calculated from STEM-HAADF)[15] has been modulated. Before Pd deposition, the CNT support has been oxidized with HNO_3 to create surface oxygen groups necessary for Pd deposition. To produce a Pd/CNT catalyst containing mainly Pd_{NP} (*catA*), we used the wet impregnation method starting from palladium nitrate precursor. For the three other catalysts, which contain increasing amounts of Pd_{SA}, we first used a thermochemical process to create carbon vacancies on the CNT support.[19] Then, we used this defective CNT support to deposit under an inert atmosphere 1.2% w/w Pd from the bis(2-methylallyl)palladium precursor (Fig. S1). According to the number of deposition cycles (4 x 0.3% Pd for *catB*; 2 x 0.6% Pd for *catC* and 1 x 1.2% Pd for *catD*), the Pd_{SA}/Pd_{NP} ratio could be modulated. In this catalyst series (*catB-D*), the Pd_{SA}/Pd_{NP} ratio decreased with increasing number of deposition cycles. The effective Pd-loading in these Pd/CNT catalysts was determined by ICP-OES (Table 1); it is close to the expected loading in all cases. The four catalysts were characterized by STEM-HAADF, X-ray photoelectron spectroscopy (XPS) and X-ray absorption spectroscopy (XAS). Fig. 2 shows representative high-resolution STEM-HAADF micrographs of the four catalysts (lower resolution micrographs where Pd_{NP} distribution is more easily visualized are shown on Fig. S2). In the catalyst series, the Pd_{SA}/Pd_{NP} ratio varied from 3 in *catA* to 108 in *catD; catB and catC* showing intermediate values (11 and 40, respectively).

4
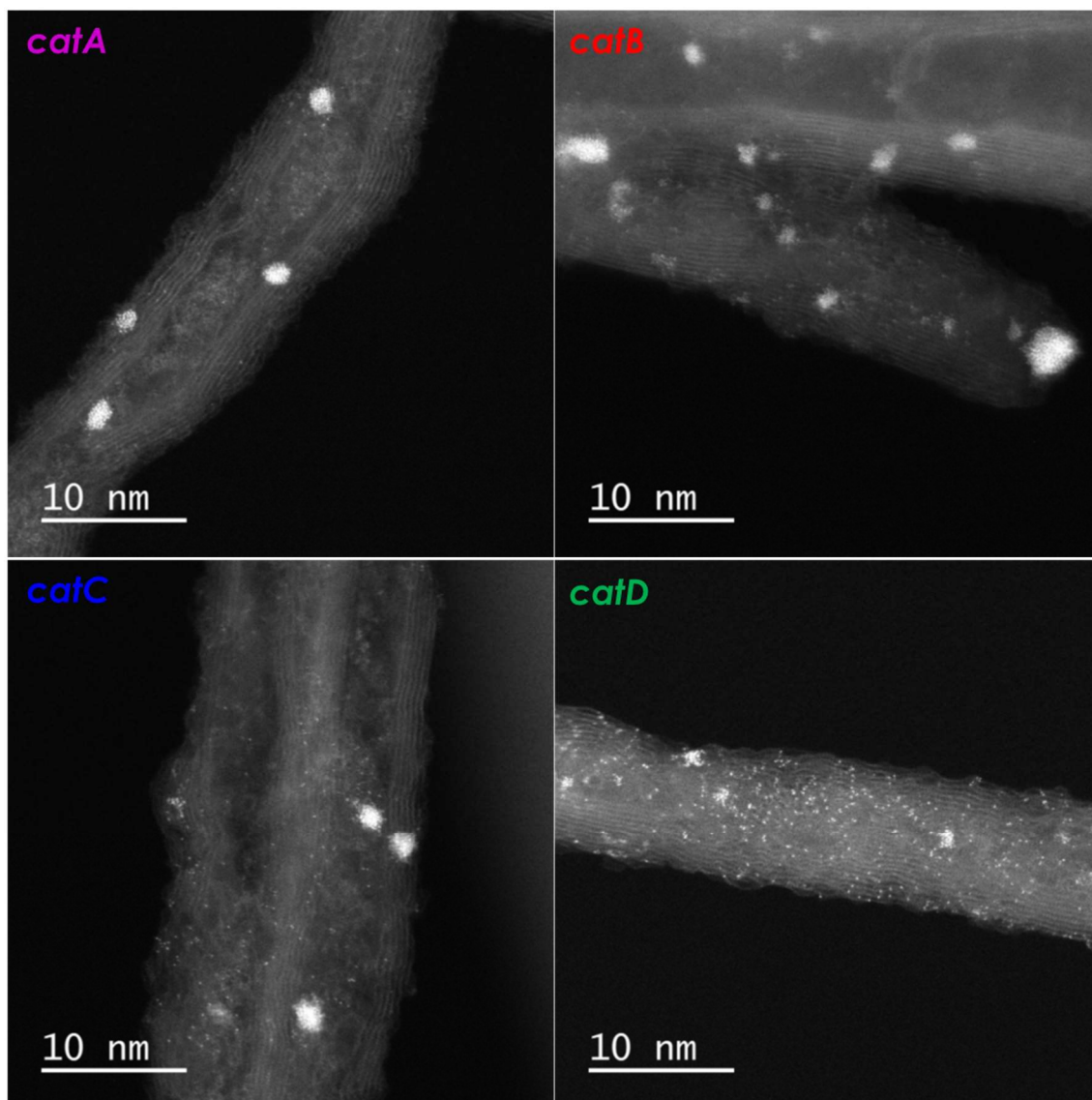
Figure 2. High-resolution STEM-HAADF micrographs of the four Pd/CNT catalysts (scale bar = 10 nm).

The Pd_{NP} size distributions based on the total number of Pd_{NP} and the total number of atoms (see ref[20] for calculations) are shown in Fig. S3. In the catalyst series (from *catA* to *catD*), the mean Pd_{NP} size is decreasing from 1.5 nm in *catA* to *ca.* 1 nm in *catD* (Table 1). The Pd dispersion is thus increasing from *catA* to *catD*. The atomic percentage of Pd_{SA} determined by STEM-HAADF followed the order: *catA* (1.8%) < *catB* (7.3%) < *catC* (18.3%) < *catD* (68.1%). As STEM-HAADF provides only a very local analysis of the samples (poor statistic value), the catalyst series was also characterized by XPS and XAS, two reference techniques for metal-supported SA characterization.[21]

XPS analyses were performed on all four samples with introduction of the samples by an Ar-filled transfer vessel from a glove box under a controlled argon atmosphere; any air oxidation of these samples can be excluded. Fig. 3 shows the deconvolution of the Pd 3d spectra of the four catalysts (results from the deconvolution are given in Table S1).

5

Table 1. Characterization of the Pd/CNT catalysts.

Catalyst	Pd loading (%)	Pd_{NP} size (nm)	D (%)	Pd_{SA}/Pd_{NP} (STEM)	$\%at_{SA}$ (STEM)	$\%at_{SA}$ (XPS)
catA	1.09	1.54 ± 0.47	66	3	1.8	21.4
catB	1.15	1.35 ± 0.52	73	11	7.3	35.0
catC	1.37	1.30 ± 0.47	76	40	18.3	45.5
catD	1.16	0.97 ± 0.27	96	108	68.1	62.5

Two contributions can unequivocally be identified. The first doublet with a Pd $3d_{5/2}$ BE between 335.6-336.2 eV is in agreement with the value reported in the literature for metallic palladium in small Pd_{NP}.[22] The second doublet with a Pd $3d_{5/2}$ BE between at 337.2-337.9 eV can be safely attributed to electron-deficient Pd_{SA},[23] experiencing significant charge transfer from the metal to the support.[24] As expected, the peak corresponding to Pd_{SA} is increasing from *catA* to *catD*, whereas the peak corresponding to Pd_{NP} is simultaneously decreasing (Fig. 3). The atomic percentage of Pd_{SA} determined by XPS followed the order: *catA* (21.4%) < *catB* (35.0%) < *catC* (45.5%) < *catD* (62.5%). These data are in good agreement with those determined by STEM-HAADF (Fig. S4), confirming the possibility to modulate the Pd_{SA}/Pd_{NP} ratio in Pd/CNT catalysts.

Fig. S5 presents the evolution of the Pd valence band states for the four catalysts (after subtraction of the contribution of the support). The centroid shift of the Pd $4d$ valence band towards high-binding energy observed for *catB*, *catC* and *catD* can be attributed to the presence of smaller Pd_{NP} in strong interaction with the support in these catalysts compared to sample *catA*.[22d, 25] The presence of a higher atomic percentage of Pd_{SA} in these samples can also be the origin of this phenomenon. Indeed, the Pd d-band center for both graphene-anchored small Pd_{NP} and Pd_{SA} has been calculated to be 2.0 and 4.6 eV, respectively.[24a] In the catalyst series, the Pd d-band center was found at 2.7±0.2 eV for *catA*, 3.7±0.2 eV for *catB*, 3.5±0.2 ev for *catC*, and 3.3±0.2 eV for *catD*.

Fig. S6 shows the XANES spectra of the four catalysts compared to the spectrum of a Pd reference foil. There is no significant shift in the edge position, indicating that the Pd atoms are in the zero-valence state in all four Pd/CNT catalysts. Moreover, the Pd foil characteristic features, *A* (1s→5p, pd at 24367 eV) and *B* (1s→4f, pf at 24390 eV), are also present in all four catalysts, *catA* being the most similar to the Pd foil, while in *catB-D* the intensity of feature *B* is reduced significantly with respect to feature *A*. The XANES spectra of *catB-D* are indeed very similar. It should be noted that there is no indication of a shift in the positions of the XANES characteristic features of the samples with respect to the Pd foil, as instead, it was observed for 7-, 12-, and 23-nm unsupported Pd_{NP} synthesized by thermal evaporation, which was attributed to a lattice contraction.[26]
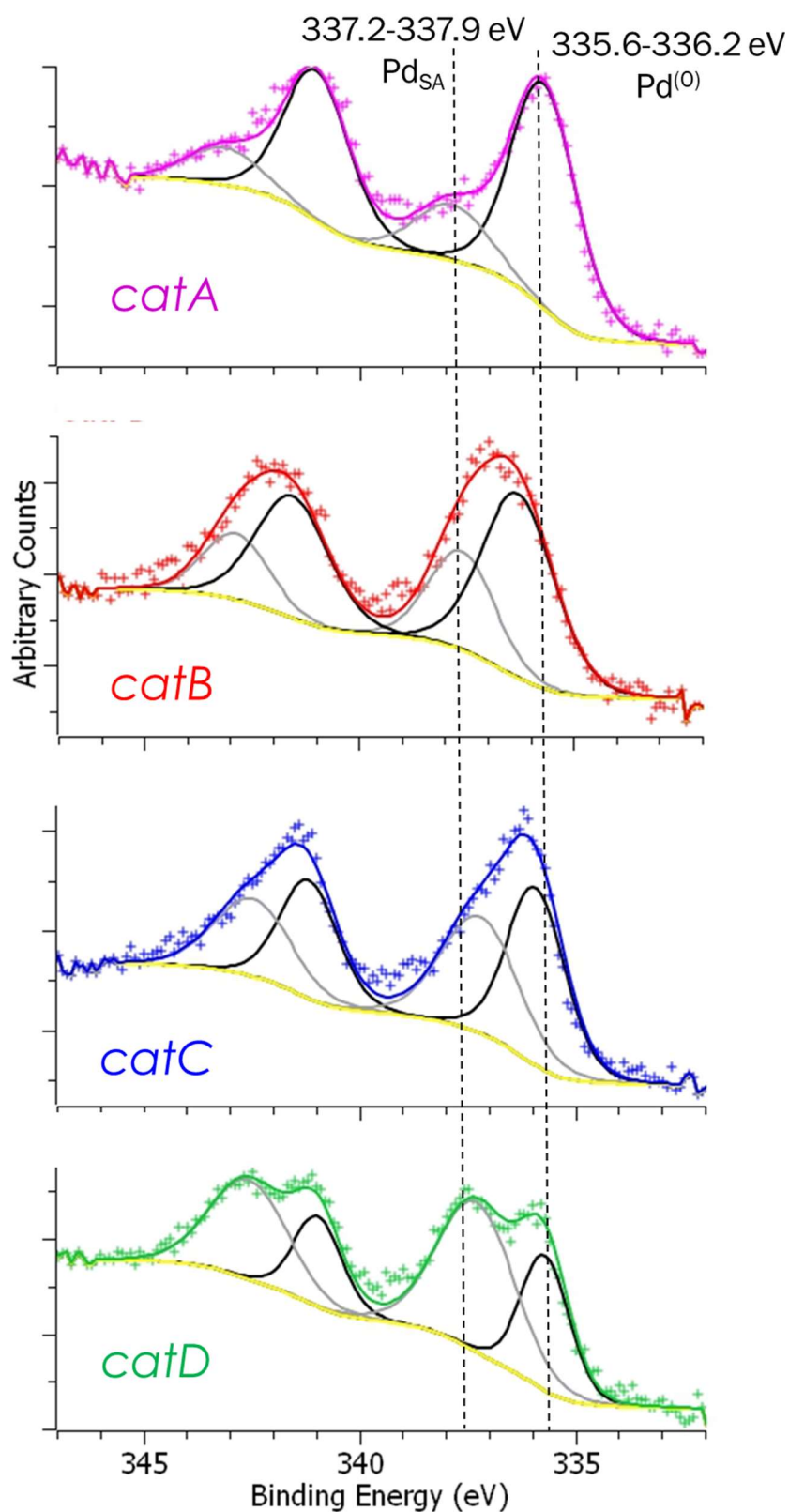
Figure 3. High-resolution Pd 3*d* XPS spectra of the Pd/CNT catalyst series.

The EXAFS $k^2\chi(k)$ and corresponding Fourier transforms (FTs) of the Pd foil and the catalysts are reported in Fig. 4a. A qualitative inspection of the $k^2\chi(k)$ shows that the oscillations of all the samples are in phase with those of the Pd foil, with *catA* being the most similar to the Pd foil, in agreement with XANES results. The FT of the Pd foil presents several peaks characteristic of its *fcc* structure, with termination ripples being observed on the left-hand side of the first Pd–Pd shell. The FT of *catA* shows a peak corresponding to the first shell of the Pd foil, with highly reduced amplitude, and shows no evidence of a peak at lower R due to Pd–C or Pd–O distances; moreover, peaks at higher R due to further Pd-Pd shells are barely detectable. These results are in agreement with *catA* containing mainly Pd_{NP} with no evident presence of Pd_{SA}. In the other samples, the peak corresponding to the first Pd–Pd shell of the *fcc* Pd structure is further reduced in amplitude. Moreover, in addition to termination ripples, the region at lower R might contain contributions due to Pd–C or Pd–O distances, which are likely due to Pd_{SA} coexisting with Pd_{NP} in *catB-D*.
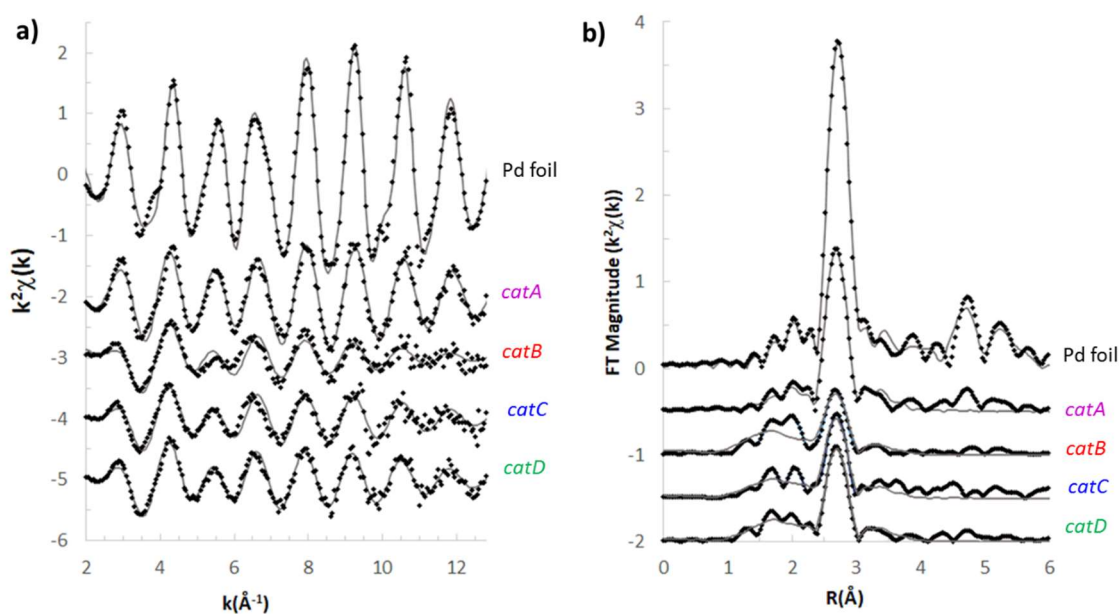
Figure 4. (**a**) EXAFS $k^2\chi(k)$; and (**b**) corresponding FTs for a reference Pd foil and for the 4 catalysts. Experiment (♦) and fit results (continuous line).

Fig. 4b also shows the fitting results, and the best-fit parameters are given in Table 2. The Pd foil was fitted using the first four shells of the known crystallographic data. For *catA* a good fitting was obtained using a single Pd–Pd shell, which is consistent with Pd being present only as Pd_{NP}, within the experimental error. The observed coordination number, significantly lower than the value expected for bulk Pd (12) is consistent with the Pd_{NP} being around 1.5 nm in size,[27] in agreement with the STEM results. For *catB-D*, the fitting is improved by adding a Pd–C shell to the Pd–Pd shell. This result, together with the further decrease in Pd–Pd coordination number in *catB-D* with respect to *catA*, points to the presence of a detectable amount of Pd_{SA} in these catalysts.

8

However, the trend observed in the EXAFS results does not agree with the STEM and XPS results. In particular, STEM and XPS indicates that *catD* is mainly made of Pd_{SA}, while EXAFS points to a significant amount of Pd_{NP} in this sample, since the Pd-Pd coordination number is larger in catD than in *catB* and *catC*. It should be noted that EXAFS is more sensitive to heavier elements, than lighter ones, which means that the Pd–Pd distances in the Pd_{NP} will dominate the results. Since EXAFS results average the entire sample, it is likely that some larger Pd_{NP} are present that STEM might not detect, contributing significantly to the overall EXAFS results. It should also be noted that the Pd–Pd distance in the samples does not indicate any contraction of the lattice that could influence their reactivity, in agreement with previous findings for Pd_{NP} supported on SiO_2 or Al_2O_3,[28] and differently from support-free Pd_{NP}.[26] This suggests the presence of a support limits lattice contraction in Pd_{NP}. The present results confirm that EXAFS is not sensitive enough to identify SAs, which may easily confuse the contributions from small clusters or NPs due to the polydispersity and disorder effects.[29]

Table 2. Best fit parameters of EXAFS data for the Pd/CNT catalyst series. Coordination numbers (N), distances (R), Debye-Waller factors, and ΔE_0. The amplitude reduction factor, S_0^2, was determined from the Pd foil best fit (0.88) and then kept fixed when fitting the data of all samples.

Catalyst	Pd–C			Pd–Pd			ΔE_0
	N	R(Å)	$2\sigma^2$ (Å^2)	N	R(Å)	$2\sigma^2$ (Å^2)	
catA	-	-	-	7.8±0.6	2.75±0.01	0.0078±0.0006	-5.7±0.6
catB	3±2	2.04±0.03	0.01±0.02	5.4±1	2.74±0.03	0.012±0.003	-6±2
catC	1±1	2.04±0.03	0.01±0.01	5.1±0.6	2.74±0.01	0.010±0.001	-6.2±0.8
catD	1.5±0.8	2.04±0.03	0.01±0.01	5.9±0.5	2.75±0.01	0.0096±0.0008	-5.7±0.7

Catalytic performances for styrene hydrogenation in batch reactor

The catalytic performance for PhA selective hydrogenation to ST was evaluated for the four catalysts at 30 °C under 5 bar H_2 in methanol. The composition profiles over time for each catalyst are given in Fig. S7. All reactions were performed up to 100% conversion. The selectivity referred to the desired product (styrene) was evaluated at three PhA conversion values (20, 50, and 90%). Three TOF values (calculated based on total surface Pd) were considered to evaluate catalyst activity: the TOF_1 (PhA→ST), the TOF_2 (ST→EB), and the TOF_{H_2} corresponding to the total H_2 consume (1 eq. for PhA→ST and 2 eq. for PhA→EB). TOF values were evaluated at three PhA conversion values (20, 50, and 90%). All the measured data for the four catalysts are reported in the Table S2 and those obtained at 90% PhA conversion are given in Table 3. The evolution of ST selectivity and the different TOFs with PhA conversion is reported in Fig. 5 for the four catalysts.

Table 3. Catalytic performance at 5 bar H_2, 30 °C in methanol. TOF were calculated based on total surface Pd.

Catalyst	$S_{ST-90\%}$ (%)	$TOF_{1-90\%}$ (s^{-1})	$TOF_{2-90\%}$ (s^{-1})	TOF_1/TOF_2	$TOF_{H2-90\%}$ (s^{-1})
catA	8	0.14	1.66	0.08	3.47
catB	32	0.71	1.50	0.47	3.72
catC	61	1.4	0.90	1.55	3.21
catD	80	0.77	0.19	4.05	1.16

From these data, it appears that *catD*, which contains the highest proportion of Pd_{SA}, is the least active (lowest TOF_{H2} whatever the level of conversion) but the more selective catalyst. In contrast, *catA* presenting the highest proportion of Pd_{NP} is by far the least selective catalyst, but not the most active. Interestingly, *catD* exhibits a higher TOF_1 than *catA* at conversion levels higher than 50% (Fig. 5b).
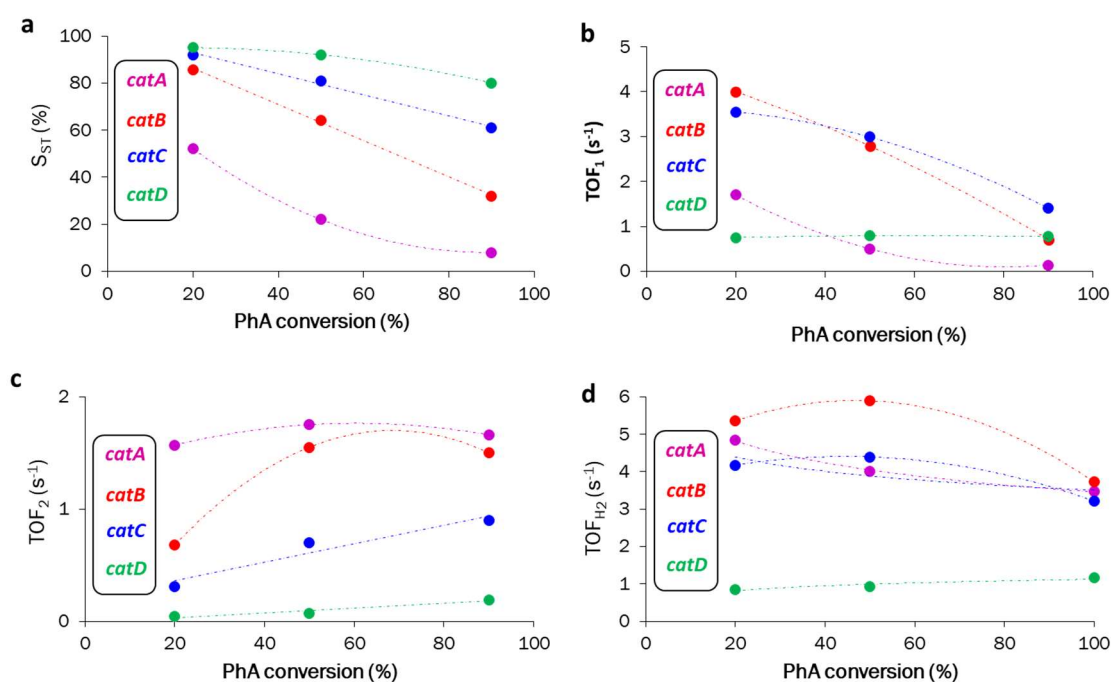
Figure 5. Evolution of S_{ST} (**a**) and of the different TOFs (**b-d**) with PhA conversion for the four catalysts. Dotted lines have been added for better monitoring of evolutions.

We independently compared the performances of *catA* and *catD* for ST hydrogenation (Table S3). *CatA* is much more active than *catD*, with measured TOF at 90% conversion of 3.48 s^{-1} (*catA*) and 0.62 s^{-1} (*catD*). This result is in agreement with our previous studies on alkene

hydrogenation.[15] *CatB* and *catC* show high activity and intermediate selectivity. The most active catalyst is *catB* when considering the TOF_{H2}. We already reported that for alkene hydrogenation, the highest activity is obtained with catalysts presenting an optimal Pd_{SA}/Pd_{NP} ratio as well as support surface functional groups involved in H-spillover.[15] Figure 6 shows the evolutions, at 90% conversion, of TOFs and S_{ST} as a function of the Pd_{SA}/Pd_{NP} ratio. The highest $TOF_{H2-90\%}$ is obtained for *catB*, presenting a Pd_{SA}/Pd_{NP} ratio = 11, a value which is consistent with our previous studies on alkene hydrogenation.[15] This optimal ratio should offer the best control for the balance between H_2 activation on Pd_{NP}, the H-spillover and Pd_{SA}-H catalyzed alkyne/alkene hydrogenation rates. It is worth noting that we were unable to find any correlation between Pd_{NP} size or Pd dispersion with the TOF data measured. We independently checked that *catB* presents the best structure for H-spillover to operate. It is known that the spilled-over H species is known to react readily under mild conditions with WO_3 (yellow powder) to form dark blue H_xWO_3.[30] Hydrogen molecules perform the reduction only above 200 °C.[31] As shown in the photographs of Fig. S8, the WO_3 alone exhibited an unchanged color after H_2 treatment for 5 min at 20 °C. When mixed with 10 mg of the Pd/CNT catalysts, changes in colors are observed, consistent with the following order for the extent of H-spillover: *catB > catA > catC > catD. CatB*, featuring a relatively low Pd_{SA}/Pd_{NP} ratio and a small Pd_{NP} size, offers the best compromise for H-spillover. Interestingly, the highest $TOF_{1-90\%}$ (PhA→ST) is not obtained with *catB* but with *catC* (Fig. 6b), which shows a higher Pd_{SA}/Pd_{NP} ratio.
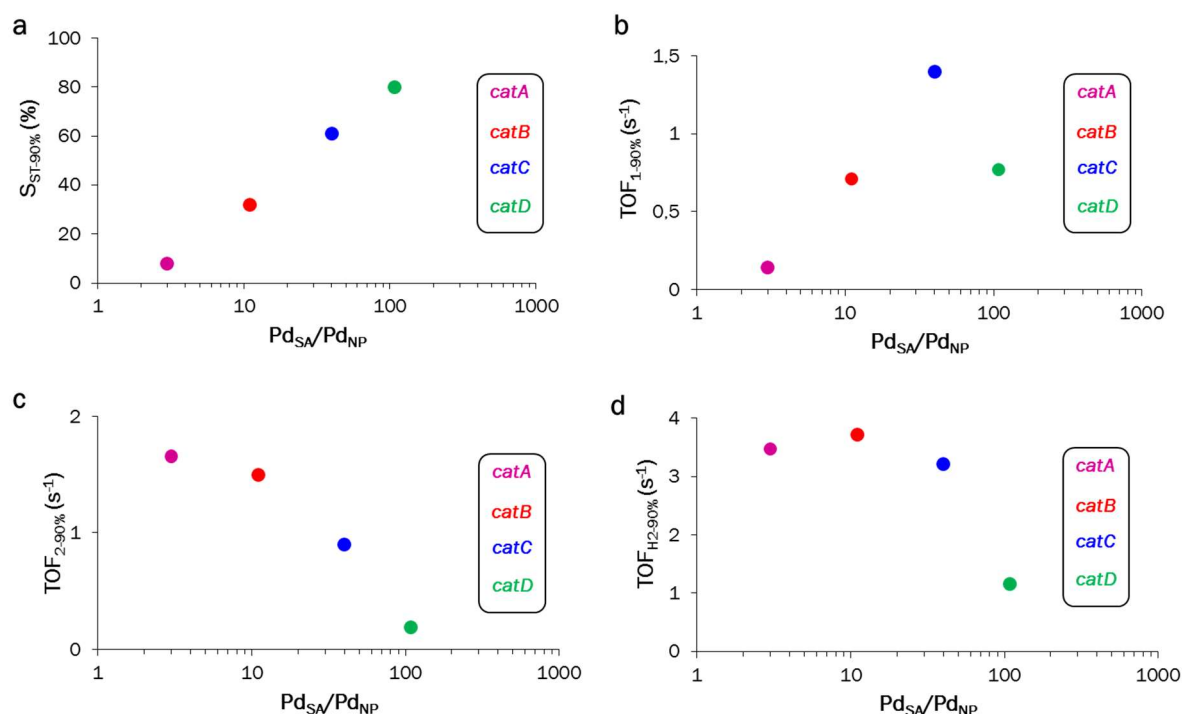

Figure 6. Evolutions of (a) $S_{ST-90\%}$ and (b-d) TOFs (at 90 % conversion) as a function of the Pd_{SA}/Pd_{NP} ratio for the four catalysts.

Fig. 5c shows the evolution of TOF_2 with PhA conversion for the four catalysts. TOF_2 regularly increases with conversion for the four catalysts (except for the most active *catA* and *catB*, for which a slight decrease is noticed at high conversion), which must be related to an increase in ST concentration in the reactor over time. Fig. 5a shows the evolution of TOF_1 with PhA conversion for the four catalysts. A more or less marked decrease is noted for the four catalysts, which is related to the activity of these catalysts: the more the catalyst is active, the more the decrease is marked.

As far as selectivity is concerned, the literature points to a higher selectivity for alkyne semi-hydrogenation on Pd_{SA}, which is however associated with poor activity due to difficulty in H_2 activation on these isolated and electron-deficient species. A 0.1% Pd_{SA}/CNT catalyst was independently prepared to evaluate its performance for ST hydrogenation. From STEM-HAADF analyses (Fig. S9), it was checked that this low-loading catalyst contains only Pd_{SA}. This 0.1% Pd_{SA}/CNT catalyst is much less active than *catD* (Table S2), for which the Pd_{SA} benefits from the cooperativity with Pd_{NP} to form Pd_{SA}-H species *via* the H-spillover. The 0.1% Pd_{SA}/CNT catalyst is also more selective than *catD*, which confirms the harmful influence of Pd_{NP} on styrene selectivity (Fig. 6a). The origin of selectivity changes in the *catA-D* series can arise from thermodynamic (thermodynamic selectivity) and/or kinetic (mechanistic selectivity) constraints (Scheme 1).
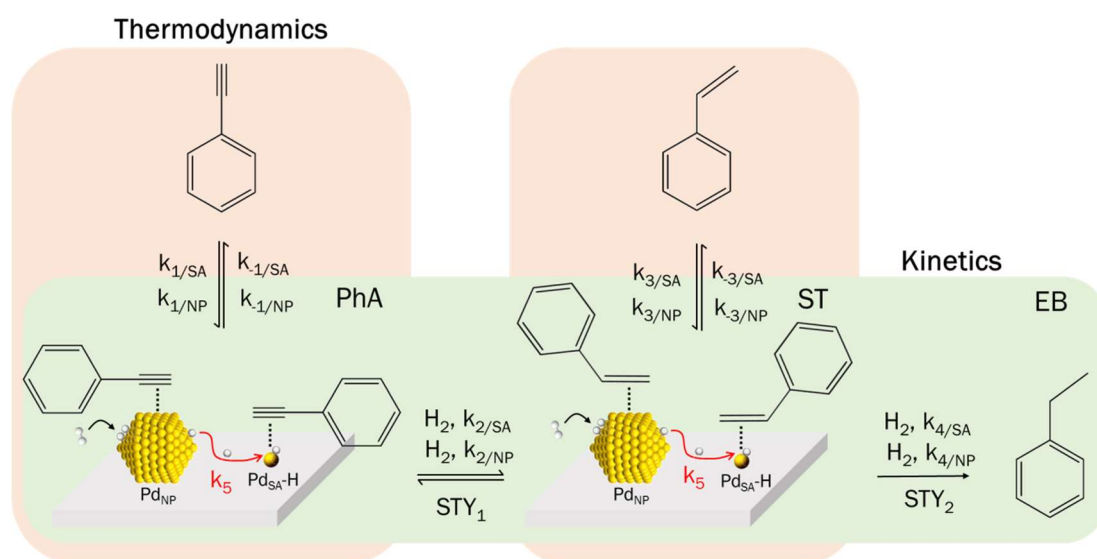
Scheme 1. General scheme of phenylacetylene hydrogenation on Pd/CNT catalysts.

The catalytic performances of the *catA-D* series indicate a significant influence of the Pd_{SA}/Pd_{NP} ratio on catalyst activity and selectivity. From this viewpoint, it is informative to analyze the effect of the Pd_{SA}/Pd_{NP} ratio on the overall reaction kinetics, TOF_1 and TOF_2 values, and TOF_1/TOF_2 ratio. Considering the cooperative catalysis between Pd_{NP} and Pd_{SA}, it is surprising at first glance that *catB*, the most active catalyst, is not also the least selective one. This could suggest thermodynamic selectivity. The evolution of styrene selectivity obtained with the four catalysts with the TOF_1/TOF_2 ratio for different PhA conversions is shown in Fig.

S10. Because of different structure sensitivity behavior for H-addition to the C≡C and C=C bonds, respectively, the TOF_1/TOF_2 ratio linearly increases with the Pd_{SA}/Pd_{NP} ratio (Fig. 7).
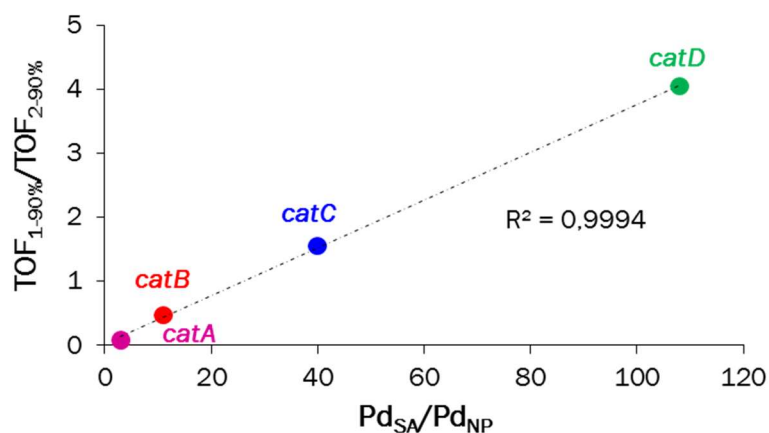

Figure 7. Evolution of the TOF_1/TOF_2 ratio with the Pd_{SA}/Pd_{NP} ratio in *catA-D*.

A parametric study in a stirred semi-batch reactor has been done with the more selective catalyst *catD* changing the nature of the solvent (methanol or hexane), the hydrogen pressure (1-10 bar), the initial concentrations of phenylacetylene (PhA/Pd = 1800-7500), and the reaction temperature (25-35 °C). Despite the fact that H_2 is more soluble in hexane than in methanol,[32] and that hexane adsorbs more weakly than methanol on palladium,[33] *catD* is more active in methanol than in hexane (Fig. S11), implying a major role of solvent polarity and proticity in promoting the catalyst activity. Contrasting results are reported in the literature regarding the effect of the solvent (alcohol or alkane) on the selective hydrogenation of PhA.[34] Interestingly, it has been shown that protic solvents such as methanol can assist the H-spillover, behaving as a shuttle for spilled over of H species.[35] The higher TOF_1/TOF_2 ratio obtained in hexane (Fig. S11) results in higher styrene selectivity in this solvent. Nevertheless, the changes in activity and selectivity observed when the catalysis is performed in hexane do not suggest a change of active species (Pd_{SA} *vs.* Pd_{NP}) because the S_{ST} observed remains high, and the TOF_{H2} low compared to *catA*. The evolution of catalytic performance descriptors with H_2 pressure, PhA/Pd ratio and temperature are shown in Fig. S12 (20% conversion) and Fig. S13 (90% conversion). The operational parametric window to achieve high styrene selectivity (Pd_{SA} regime) is relatively narrow and lies between 1-5 bar H_2, 20-30 °C, and 2000 < PhA/Pd < 8000. Analyzing initial rates is always useful for understanding the dependence of the reaction rate on individual parameters. In the Pd_{SA} regime, the rate and S_{ST} are weakly dependent on the P_{H2} and PhA concentration, suggesting that the H-spillover (k_5, Scheme 1) could be rate-limiting. The change in kinetic regime results in a sharp increase in TOF_{H2}, a decrease in the TOF_1/TOF_2 ratio, and a marked drop in styrene selectivity. The regime change occurs for a hydrogen pressure > 5 bar or when the PhA concentration is low. The effect of temperature on the change of kinetic regime is also evident as soon as T exceeds 30 °C.

Mechanistic studies on the Pd$_{NP}$-Pd$_{SA}$ system

DFT calculations were carried out to analyze the thermodynamic and/or kinetic constraints that lead to the resulting differences in catalytic performances. For this, the model of the previously described Pd$_{NP}$-Pd$_{SA}$ catalyst is first considered,[24a] which includes the two metal species of interest, the Pd atoms of the Pd$_{NP}$ and the Pd$_{SA}$ located in a monovacancy, (PdC$_3$)$_{SA}$.

To better understand the experimental investigations, the reaction mechanism for the complete hydrogenation of PhA to ST and EB on the two metal species of the Pd$_{NP}$(PdC$_3$)$_{SA}$ catalyst model is studied. Starting from the role of palladium in Pd$_{NP}$, the coordination of methanol as reaction solvent is first considered (Fig. S14a), which results in a weak adsorption energy of about -12 kcal·mol^{-1}. Next, the energy profile and corresponding structures are summarized in Fig. 8 (most favorable mechanisms), Fig. S15 (complete hydrogenation pathways), and Fig. S16, respectively. The energy profiles are presented as potential energies, consequently, without considering the entropies.

In **1** (representing the model catalyst Pd$_{NP}$(PdC$_3$)$_{SA}$), the reaction initiates with a π coordination of the alkyne function of PhA. The organic substrate strongly adsorbs on the Pd$_{NP}$ surface (**2$_{CCH}^{NP}$** at -39.1 kcal·mol^{-1}, see Fig. 8, Fig. S15 and Fig. S16), so in the presence of PhA the solvent molecules adsorbed on the Pd should be easily replaced by the substrate. Because the carbon atoms of the triple bond have different connectivity, the first addition of H is considered on both atoms additionally for all cases studied. Furthermore, given the high H-coverage conditions, where there are several H atoms around PhA, the H that attacks the organic moieties is always the closest. Starting from **2$_{CCH}^{NP}$**, the first hydrogenation step is essentially a thermoneutral process, the terminal ≡CH carbon being the most likely to be reduced with a reaction energy of -1.1 kcal·mol^{-1} (**2$_{CCH_2}^{NP}$**, red pathway in Fig. 8). With an energy barrier (E$_{a1}$) of 18.7 kcal·mol^{-1}, the first step is reasonably achievable from the kinetic point of view. Both thermodynamics and kinetics are greatly favored in the second addition of H (**2$_{CHCH_2}^{NP}$**), with a drop in the energy barrier to only 1.4 kcal·mol^{-1}. Once ST is obtained, it remains strongly coordinated to the surface (desorption energy around 25 kcal·mol^{-1}) due to the interaction of Pd$_{NP}$ with the newly formed C=C double bond through π coordination. Thus, it is expected that the ST hydrogenation process can continue to operate due to the high activity of the Pd$_{NP}$. After recharging the catalyst under H$_2$ pressure through a thermodynamically favorable process, the third H addition takes place similarly to the first, resulting in an almost thermoneutral process although with a significantly lower energy barrier of 11.6 kcal·mol^{-1} (**3$_{CH_2CH_2}^{NP}$**, orange pathway in Fig. 8).
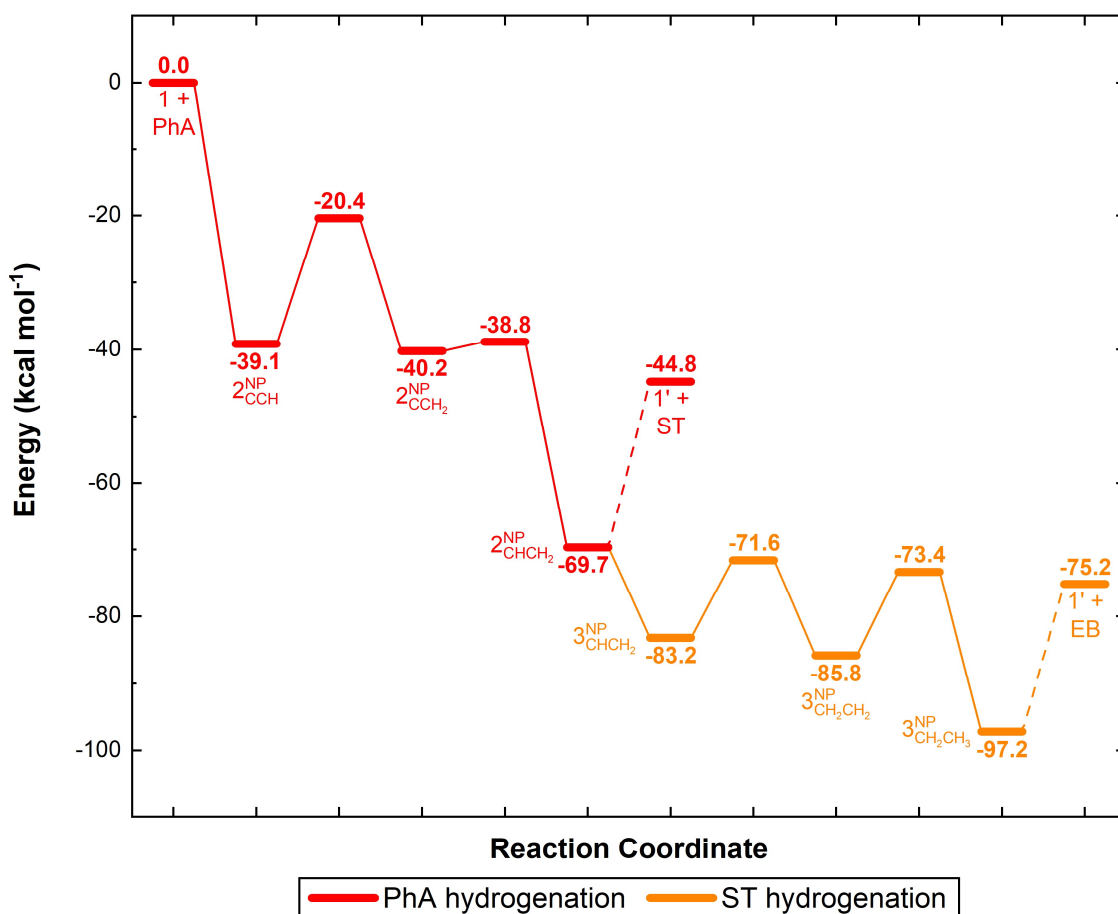
Figure 8. Reaction profile of PhA hydrogenation to ST (in red) and EB (in orange) on the Pd_{NP} of the $Pd_{NP}(PdC_3)_{SA}$ catalyst model. The energy is referenced with respect to the hydrogenated Pd-supported catalyst (1) and $PhA_{(g)}$.

The low selectivity of Pd_{NP} is therefore explained by the fact that styrene will be more easily hydrogenated than desorbed from Pd_{NP}. The hydrogenation of the unsaturation is completed with the fourth and last addition of H ($3^{NP}_{CH_2CH_3}$), a step driven by thermodynamics (reaction energy of -11.4 kcal·mol^{-1}) and kinetics (energy barrier of 12.4 kcal·mol^{-1}, E_{a2}). Finally, EB is desorbed from Pd_{NP} with a slightly high desorption energy of 22 kcal·mol^{-1} (Fig. 8) due to the interaction of Pd_{NP} with the aromatic ring. Therefore, complete hydrogenation of PhA is clearly achievable on Pd_{NP}. The catalyst is highly active due to the strong adsorption energies and the low energy barriers evidenced. Although the first hydrogenation is the most energy-demanding step, the overall process entails a poor selectivity against the semi-hydrogenation from PhA to ST, in agreement with the experimental results.

Regarding the role of palladium in the isolated $(PdC_3)_{SA}$ of the $Pd_{NP}(PdC_3)_{SA}$ system, the methanol adsorption on the $(PdC_3)_{SA}$ and $(PdC_3)_{SA}$–H species is -30.3 and -26.2 kcal·mol^{-1}, respectively (Fig. S14b), significantly higher than that on Pd_{NP}. Subsequently, the energy profiles and corresponding structures are summarized in Fig. S17 and Fig. S18, respectively. As experimentally evidenced, the formation of the active species $(PdC_3)_{SA}$–H by means of an H-spillover process (1_H) turned out to be subtly favorable from thermodynamics (spillover

energy of -2.8 kcal·mol^{-1}). After a favorable adsorption along a η^2(C≡C) mode of the PhA triple bond ($\mathbf{2^{SA}_{CCH}}$, binding energy of -25.1 kcal·mol^{-1}), the reduction from triple to double bond is a thermodynamically very favorable process, with the overall reaction energy being -52.1 kcal·mol^{-1}. The most energy-demanding step is the second addition of H (energy barrier of 13.3 kcal·mol^{-1}, wine pathway in Fig. S17), which proceeds exclusively using molecular H$_2$. This result is consistent with the high TOF$_1$ measured in samples presenting a high Pd$_{SA}$/Pd$_{NP}$ ratio (Fig. 6b). Therefore, these evidences show conclusively the production of the alkene compound on (PdC$_3$)$_{SA}$–H. However, the (PdC$_3$)$_{SA}$ species remained active for plausible complete hydrogenation to EB, similar to what occurred on Pd$_{NP}$. While the desorption energy of ST is 27.7 kcal·mol^{-1}, the energy barrier for the third H addition turned out to be only 6.7 kcal·mol^{-1}, indicating non-competitive processes where the second is clearly advantaged. The C=C double bond can therefore be reduced to saturation in a second hydrogenation process, also favored from the thermodynamic point of view (global reaction energy of -31.7 kcal·mol^{-1}) and kinetic (energy barrier of 12.7 kcal·mol^{-1}, orange pathway in Fig. S17). These results are in agreement with what was elucidated in previous works for the hydrogenation of unsaturated compounds on Pd catalysts supported on nanostructured carbons.[15, 36] For all these reasons, although there is a need for the H-spillover phenomenon to operate for the (PdC$_3$)$_{SA}$ active site (unpromoted (PdC$_3$)$_{SA}$ are scarcely active), the thermodynamic and kinetic behavior is similar to that shown by Pd$_{NP}$. Based on a high activity and a low selectivity for the semi-hydrogenation reaction, these results do not allow explaining the experimentally observed selective hydrogenation.

Since the coordination sphere of isolated metal single atoms regulate their electronic structure and consequently their intrinsic catalytic performances,[37] an alternative coordination environment was explored for the Pd$_{SA}$. Due to the oxygen functional groups present on the carbon support, the possibility of O-coordination environment could be given to the (PdC$_3$)$_{SA}$ species. In this case, the proposed adsorption site is modeled by replacing one of the three C atoms that make up the single vacancy where the Pd$_{SA}$ is anchored with an O atom, resulting in a novel oxygen-decorated (PdC$_2$O$_1$)$_{SA}$ coordination structure. This Pd$_{SA}$ preserves two covalent bonds to neighboring carbons, in addition to interaction with oxygen (average Pd–C and Pd–O bond length of 1.97 and 2.69 Å, respectively, *vs.* 1.95 Å in the tricoordinate carbon system). It is also displaced outward by 1.38 Å from the graphitic surface (*vs.* 1.00 Å in the initial catalyst model), probably due to loss of a covalent Pd–C bond and the weak Pd–O interaction. The *d*-band center of Pd (ε_d, calculated as the normalized, energy-weighted integral of the DOS and projected onto all *d* AOs), governed by the local geometry and material composition, is calculated to be 2.8 *vs.* 4.6 eV of the original system, so a different contribution in the catalytic performance of the metal is to be expected. Moreover, a change in the partial atomic charge of the Pd atom is observed when analyzing the electronic distribution, undergoing an oxidation process that makes it formally have an atomic charge of +0.5 compared to +1 for the pristine (PdC$_3$)$_{SA}$ system. Experimentally, it was shown by the XANES spectrum of *catD* (highest Pd$_{SA}$/Pd$_{NP}$ atomic ratio) that the Pd atoms are in the zero-valence state, in addition to the best fit Pd–C coordination number and distances of the EXAFS data are 1.5±0.8 and 2.04±0.03, respectively (see Table 2), which gives the Pd–C$_2$O$_1$

coordination environment better similarities than the single vacancy based exclusively on carbon.

From thermodynamics, the complete phenomenon of H-spillover from Pd_{NP} to $(PdC_2O_1)_{SA}$ became appreciably endothermic (spillover energy of 9.8 kcal·mol⁻¹, see Fig. S19). However, when examining the arrival of H atoms to the neighboring carbons in the isolated Pd−C_2O_1 coordination environment, the process turned out to be feasible for some well-defined positions. The most stable were those in which hydrogen is in the *para* position of the six-membered carbon ring with respect to the metal (due to a suitable electronic rearrangement), as well as in the *meta* position of the oxygen-containing ring and closest to Pd (causing a slight activation of the C−H bond). Therefore, these structures were examined as an efficient hydrogen source for the reduction of PhA to ST and EB on the $(PdC_2O_1)_{SA}$ metal site.

Concerning the role of $(PdC_2O_1)_{SA}$ in the $Pd_{NP}(PdC_2O_1)_{SA}$ model, no significant differences were observed for methanol adsorption with respect to the pristine $(PdC_3)_{SA}$ (adsorption energy of -28.3 kcal·mol⁻¹, see Fig. S14c). Subsequently, the energy profiles and corresponding structures are summarized in Fig. 9 (most favorable mechanisms), Fig. S20 (complete hydrogenation pathways), and Fig. S21, respectively. Starting from **4** (representing the $Pd_{NP}(PdC_2O_1)_{SA}$ catalyst model), the H-spillover process at the beginning of the reaction (**4$_H$**) is still essential to operate, relatively more favorable in this coordination environment based on the above discussion. The lack of Pd−H species led to an enhanced electron density on Pd atoms (a single Pd atom is usually an electrodeficient species), which facilitated the adsorption of PhA (**5$_{CCH}^{SA}$**, binding energy of -37.5 kcal·mol⁻¹). The π coordination of the PhA is very similar to those previously found in Pd_{NP} and $(PdC_3)_{SA}$. Once PhA has been adsorbed, the possibility of first hydrogenating on one or the other carbon of the alkyne group opens up again. From a thermodynamic point of view, the reduction from triple to double bond turned out to be overall a very exothermic process, with the terminal carbon being preferentially hydrogenated in the first addition of H (**5$_{CCH_2}^{SA}$**, red pathway in Fig. 9). The importance lies in the reaction kinetics. With a first energy barrier of 37.2 kcal·mol⁻¹, the hydrogenation of the first C atom is the most energy-demanding step, and could also be considered on the limit to occur under operating conditions (1-5 bar H_2 and 20-30 °C), presumably due to the strength of the C−H bond compared to the Pd−H bond. Although the second energy barrier that leads to the formation of ST (**5$_{CHCH_2}^{SA}$**) is more accessible (19.5 kcal·mol⁻¹), the process is globally slowed down. This result is less consistent with the high TOF_1 measured in samples presenting high Pd_{SA}/Pd_{NP} ratio (Fig. 6b).

On the other hand, the desorption of ST from $Pd(C_2O_1)_{SA}$ entailed an energy cost of around 33 kcal·mol⁻¹, being less costly than the second hydrogenation process through a third addition of H (energy barrier of 40.0 kcal·mol⁻¹, dark yellow pathway in Fig. 9). The calculations elucidated that both the thermodynamics and the kinetics of the second hydrogenation are less favorable than the first. These results would allow us to understand the higher selectivity to ST observed experimentally against active Pd_{NP} species, and further reinforce the specific reactivity of Pd_{SA} experiencing O-coordination.
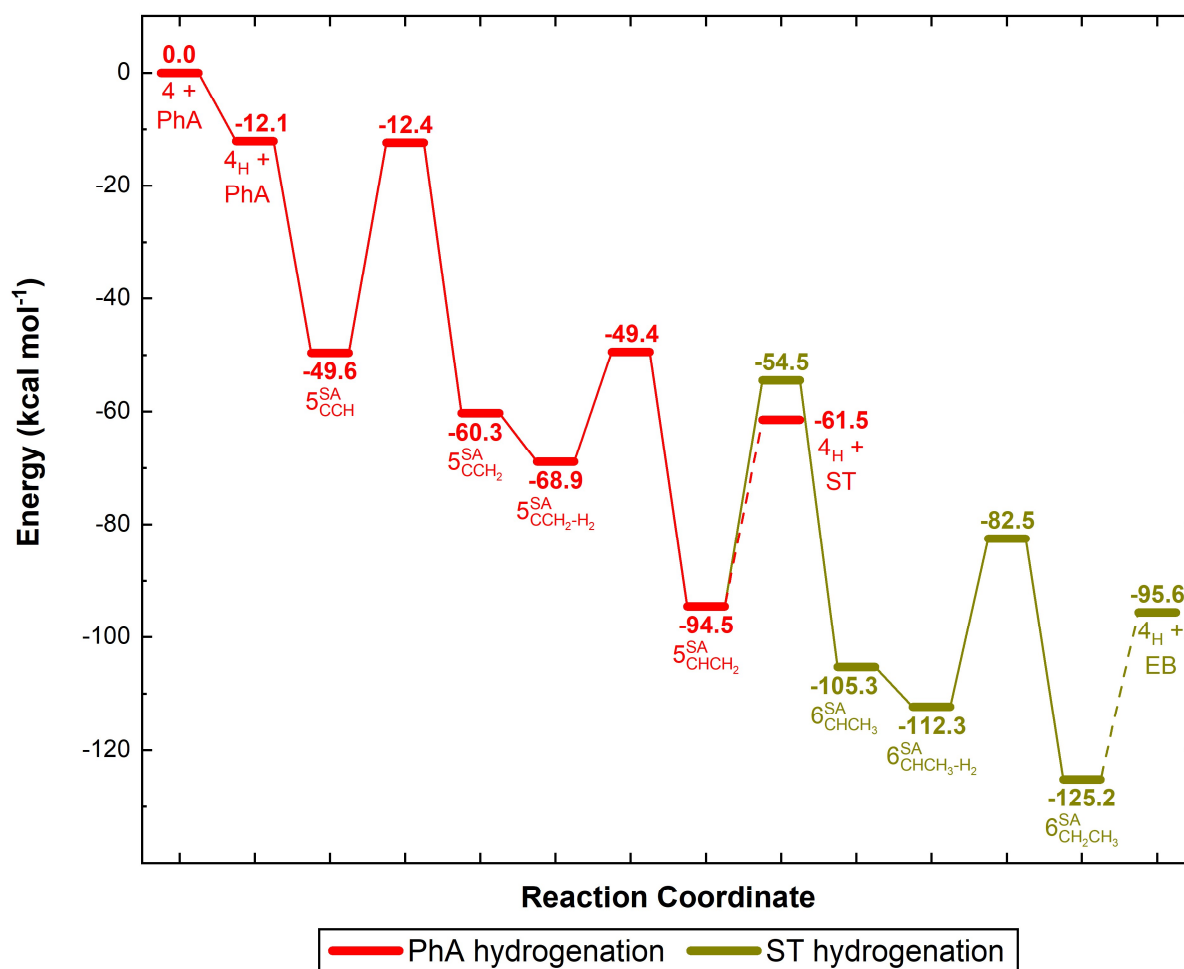
17

Figure 9. Reaction profile of PhA hydrogenation to ST (in red) and EB (in dark yellow) on the Pd_{SA} of the $Pd_{NP}(PdC_2O_1)_{SA}$ catalyst model. The energy is referenced with respect to the hydrogenated Pd-supported catalyst (4) and $PhA_{(g)}$.

Overall, this modeling study makes it possible to conclude about the reactivity of the samples presenting a low Pd_{SA}/Pd_{NP} ratio, but is not sufficient to explain the reactivity of the samples presenting a high Pd_{SA}/Pd_{NP} ratio. According to DFT, samples presenting mainly Pd_{NP} should show moderately high activity (E_{a1} = 18.7 kcal·mol^{-1} and E_{a2} = 12.4 kcal·mol^{-1}, Fig. S22) but poor selectivity, in agreement with the experimental results. The modeling study reveals above all the importance of the first coordination sphere of the Pd_{SA}. A C_3 environment leads to a system in which hydrogen spillover and high reactivity are feasible (E_{a1} = 13.3 kcal·mol^{-1} and E_{a2} = 12.7 kcal·mol^{-1}, Fig. S22), as experimentally observed. Nevertheless, the thermodynamics of PhA and ST adsorption on activated or non-activated Pd_{SA} cannot explain the high selectivity observed experimentally at high Pd_{SA}/Pd_{NP} ratio. A C_2O environment leads to a system in which hydrogen spillover is constrained, resulting in poor activity (E_{a1} = 37.5 kcal·mol^{-1} and E_{a2} = 33 kcal·mol^{-1}, Fig. S22), as observed experimentally for the pure 0.1% Pd_{SA}/CNT catalyst. However, in this case, kinetics and thermodynamics can explain the high selectivity observed experimentally at high Pd_{SA}/Pd_{NP} ratio.

Operability of the Pd/CNT catalysts in continuous flow

Finally, *catC* and *catD* were wash-coated on metallic open-cell solid foam structures to operate these catalysts in continuous flow mode. Such a "batch to continuous" transposition contributes to evaluate their stability, but also deserves an interesting demonstration for alternative reactor operation with these catalysts.[36b, 36c] Optical photographs (Fig. S23) and SEM analysis (Fig. S24) confirm a relatively uniform coverage of the structures, with an average catalyst layer thickness of 10-15 μm, in good agreement with the theoretical estimations based on weighing.

Fig. 9 depicts typical results obtained for wash-coated *catC* (Fig. 10a-b) and *catD* (Fig. 10c-d) catalysts in continuous flow experiments for different liquid flow rates and contact times. Because of the similar catalyst content, a direct comparison of the conversion/selectivity levels for the two flow experiments is possible. For an identical flow rate, *catC* presents a higher conversion than *catD*, indicating a higher activity. This result is in agreement with previous batch experiments (Fig. 5). Comparison of selectivity *vs.* conversion profiles indicates that *catD* maintains high selectivity at relatively high conversion, whereas ST selectivity decreases for *catC* at similar conversion. This is again in agreement with batch experiments (Fig. S7). These similar behaviors indicate that the wash-coating procedure does not alter the nature and performance of the catalyst. Both wash-coated catalysts exhibit good stability for all liquid flow rates.

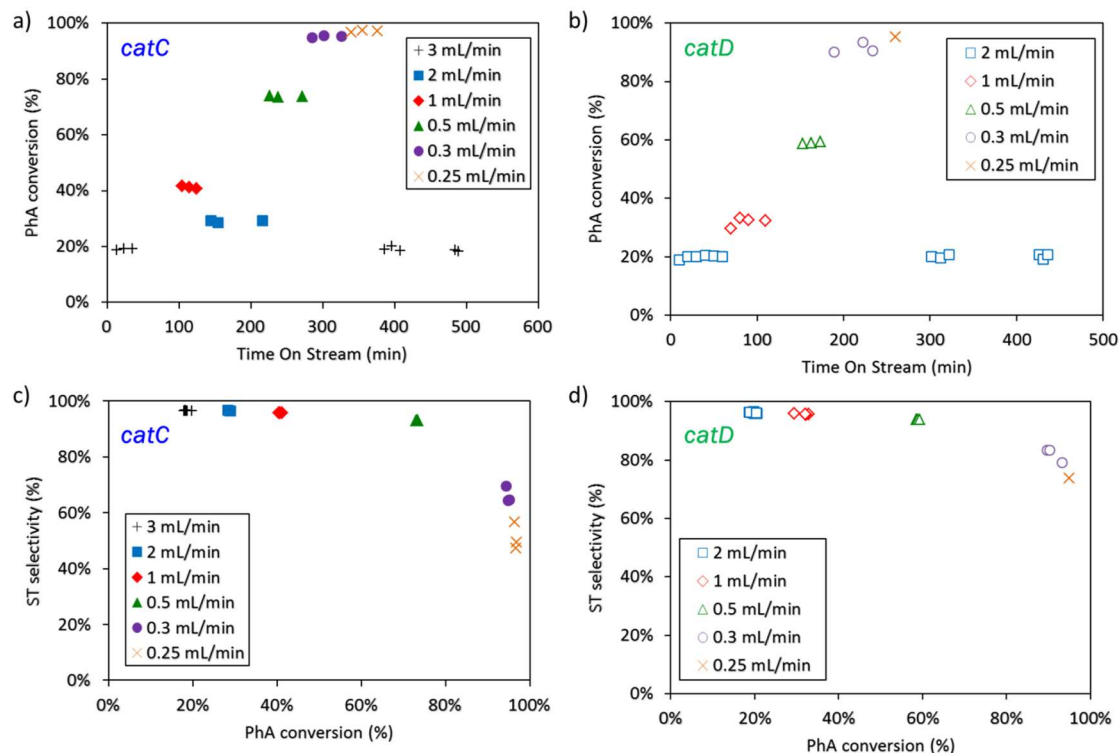**Figure 10**. Continuous flow experiments of PhA partial hydrogenation (30 °C, 5 bar 20 N mL min^{-1} H$_2$). (**a-b**) Time on stream evolution of PhA conversion for *catC* and *catD*; (**c-d**) selectivity *vs.* conversion profiles for *catC* and *catD*.

Control experiments carried out at the initial flow rate at the end of the sequence confirms this good stability, returning to the same conversion. To quantitatively appreciate the work of the catalyst, Turn Over Numbers (TON, in $mol_{PA}\ mol_{Pd}^{-1}$) were calculated through each flow experiment. The *catC* and *catD* samples reach relatively high TON levels, 13500 and 8800, respectively, without any noticeable deactivation.

The PhA conversion and ST yield evolutions are plotted against contact time (s $mol_{Pd}\ mol_{PhA}^{-1}$) in Fig. 11 for both catalysts. This figure clearly shows pseudo-zeroth order kinetic behavior for these two catalysts at PhA conversions less than 90%. Regarding ST yields, *catD*, which presents the highest SA/NP ratio, can reach a maximum yield of 75%, whereas it remains around 68% for the most active *catC* with the lowest SA/NP ratio. This again is in reasonable agreement with previous results obtained in the batch reactor, since the $S_{ST-90\%}$ was 80% for *catD* and 61% for *catC*. The fact that *catC* behaves slightly better in flow could be related to the widely spaced samples in batch experiments, which do not allow capturing the optimal point.
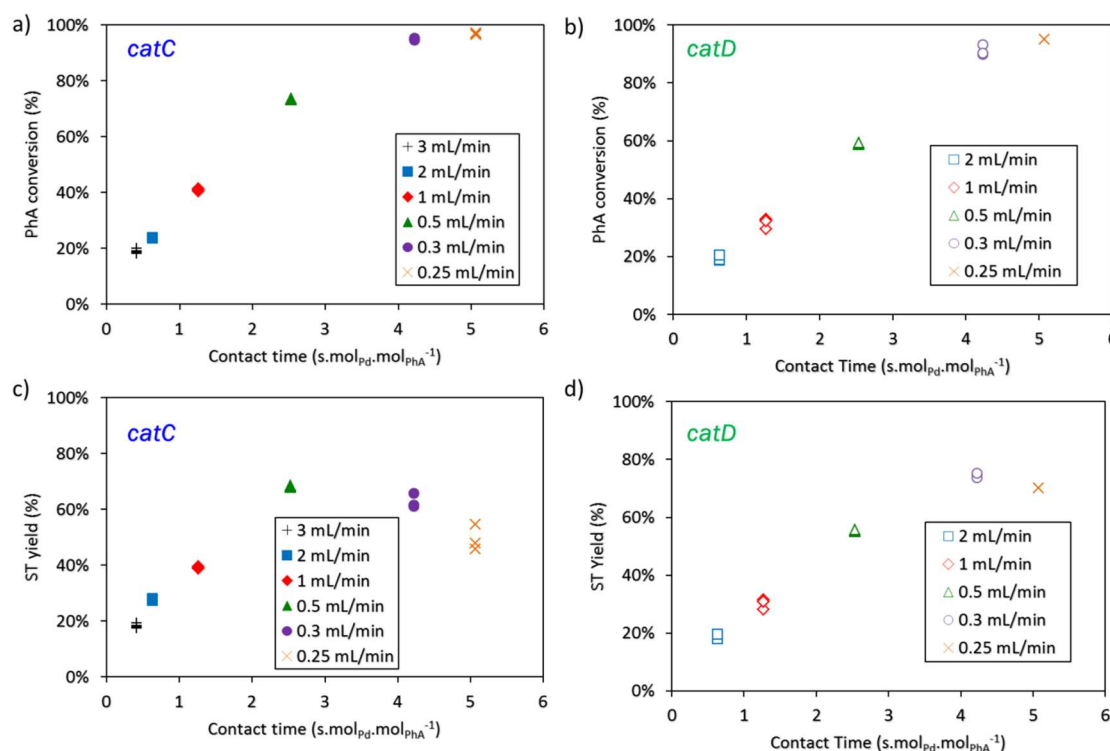
Figure 11. Continuous flow experiments of PhA partial hydrogenation. PhA conversions (**a-b**) and ST yields (**c-d**) *vs.* contact time profiles for *catC* (**a**, **c**) and *catD* (**b**, **d**).

Conclusion

A series of CNT-supported Pd catalysts presenting different proportions of Pd_{SA} and Pd_{NP} (for identical metal loading) have been prepared and characterized. Although STEM and XPS analyses make it possible to propose a coherent order in the Pd_{SA}/Pd_{NP} ratios, this study

confirms that EXAFS can show some limitations for the characterization of such systems. In the series of catalysts, the mean Pd_{NP} size decreases with increasing Pd_{SA}/Pd_{NP} ratio. The experiment showed that hydrogen spillover is possible in these systems, and that its intensity decreases at high Pd_{SA}/Pd_{NP} ratios. For the selective hydrogenation of PhA in semi-batch mode, it is shown that a low Pd_{SA}/Pd_{NP} ratio results in active but poorly selective catalysts. Increasing this ratio results in increased selectivity to styrene, but not decreased activity, as is generally observed in PhA hydrogenation. The most selective catalyst is the one presenting the highest proportion of Pd_{SA}, while the most active one presents an optimal Pd_{SA}/Pd_{NP} ratio, which allows a good balance between hydrogenation and H-spillover. The more selective catalysts were also successfully implemented in continuous flow. DFT calculations revealed that the selective hydrogenation of PhA to ST is a highly exothermic reaction, kinetically accessible only by Pd_{SA} presenting an oxygen atom in their first coordination sphere. The Pd_{NP} species is more active but much less selective than any Pd_{SA} active site, favoring complete reduction to EB via a kinetically viable pathway. In $(PdC_2O_1)_{SA}$, the most energy-demanding step for the triple to double bond hydrogenation reaction (37.2 kcal·mol^{-1}) is notably higher than that of $(PdC_3)_{SA}$ (13.3 kcal·mol^{-1}). Modifying the single vacancy where Pd_{SA} is deposited greatly increased the barriers needed for H addition, contributing to lower activity but high selectivity. Overall, this study reveals the importance of a good understanding of the first coordination sphere of Pd_{SA} to rationalize their catalytic performance.

Materials and methods

Pd/CNT catalyst preparation

The catalyst *catA* was prepared using the dry impregnation method. The desired amount of palladium(II) nitrate solution [$Pd(NO_3)_2 \cdot 2H_2O$] was added to acetone (10 mL) containing 1 g of CNTs to yield 1.2 wt% Pd. The solution was sonicated at room temperature for 1 hour and magnetically stirred overnight. The solution was then filtered and washed with acetone. The resulting solid was dried in an oven at 120 °C overnight. Finally, the catalyst was reduced in a horizontal tube furnace under a flow of argon and hydrogen (20 vol% H_2) at 300 °C for 2 h (10 °C min^{-1}).

The three 1.2% Pd/CNT catalysts *catB-D* with different Pd_{SA}/Pd_{NP} ratios were produced according to a published procedure using the bis(2-methylallyl)palladium precursor (Fig. S1).[15, 19] Briefly, homemade CNTs[36a] were first oxidized with HNO_3 under reflux at 140 °C for 3 h. The solution was filtered, and the oxidized CNTs were washed with distilled water until the pH stabilized at around 6. The solid was dried in an oven at 80 °C overnight. The oxidized CNTs (S_{BET} = 220 m^2 g^{-1}) were heated under Ar up to 400 °C during 1 h, and then cooled down at *rt* under Ar. The CNTs were transferred to a Schlenk tube under Ar. Separately, the desired amount of Pd precursor was dissolved in 30 mL of degassed pentane under argon. The solution was mixed with the support and let to react for 1 h at *rt* under Ar. Afterward, the solid was filtrated, washed three times with pure pentane, and dried under vacuum. Finally, the sample was heated up to 80 °C for 1 h under an 80/20 Ar/H_2 gas mixture. The sample *catB* was

produced with 4 deposition cycles, *catC* with 2 deposition cycles, and *catD* with a single deposition cycle.

The 0.1% Pd_{SA}/CNT catalyst containing exclusively Pd_{SA} was prepared by the wet impregnation method. The desired amount of palladium(II) nitrate dihydrate [$Pd(NO_3)_2 \cdot 2H_2O$] was added to an acetone solution (100 mL) containing 1 g of oxidized CNTs, to introduce 0.1% w/w of metal. The solution was sonicated at *rt* for 6 h using an ultrasonic finger. Subsequently, it was filtered, and the solid was washed with acetone and dried in an oven at 120 °C. Finally, the catalyst was reduced in a horizontal tube oven under an argon and hydrogen flow (20 vol% H_2 in argon) at 300 °C for 2 h.

Coating of open-cell solid foam substrates with Pd/CNT catalysts

NiCr metallic open-cell solid foams (RECEMAT NC2733) were precisely cut into cylinders (diameter: 4.3 mm and length: 25.0 mm) through electric arc discharge machining. Foam pieces were degreased in acetone under sonication for 15 min, and dried overnight. Then, the cleaned substrates were activated thermally (5 °C min^{-1}, 4 h plateau at 600 °C, natural cooling down to ambient temperature) under air atmosphere. The activated foam pieces were then dip-coated with a water suspension (60 g L^{-1}) of the Pd/CNT catalyst following an already described procedure adapted from our previous works.[36b, 38] The excess suspension was removed by air blowing through the coated structures. The samples were then dried overnight at 80 °C and weighed. *CatC* and *catD* were coated according to this procedure. Similar catalyst loadings of 28.0 ± 3.0 g_{cat} L_{foam}^{-1} were obtained for the different foam pieces, corresponding to an estimated mean layer thickness of around 15 µm (assuming a homogeneous coverage). Coating homogeneity was characterized through optical microscopy (Keyence VHX-6000), and SEM-EDX measurements helped confirm the coating's mean thickness.

Characterization

Elemental analyses were carried out on a Perkin Elmer 2400 Serie II elemental analyzer. The Pd content in the Pd/CNT catalysts was measured by inductively coupled plasma optical emission spectroscopy (ICP-OES) with a Thermo Scientific ICAP 6300 instrument. The high-resolution microscopy analyses were conducted using a JEOL JEM 2100F equipped with a field emission gun (FEG) operating at 200 kV with a point resolution of 2.3 Å and a JEOL JEM-ARM200F Cold FEG operating at 200 kV with a point resolution of > 1.9 Å. The particle size distribution was determined by manually measuring enlarged micrographs from different areas of the TEM grid (at least 300 particles). The reported size distribution in atomic percent Pd (based on the total number of atoms) in each size range was obtained by calculating the number of atoms (N) in each nanoparticle assuming a spherical shape using of an equation described in the literature.[20] The Pd_{SA}/Pd_{NP} ratio (a number ratio) was measured from the STEM-HAADF analyses of at least 500 elements. The dispersion of Pd was calculated from a universal mathematical relationship between the average relative size of metallic crystallites and their dispersion.[39] X-Ray photoelectron spectra were recorded on a Thermo Electron Kα apparatus with a base pressure of 5·10^{-9} mbars. The incident photon energy was 1487 eV (Al Kα). For high-resolution acquisition, the analyzer was set in CAE mode with pass energy of 20 eV. Data processing was performed using CASAXPS.

The X-ray absorption spectra were recorded on the B18 beamline at the DIAMOND synchrotron (Oxfordshire, UK). The samples, in the form of powder, were diluted with polyvinylpyrrolidone (PVP) inside a glove box and pressed to form a pellet, which was then sealed in an aluminum pouch to avoid any oxidation. Spectra at the Pd (24350 eV) K-edge were collected at room temperature in fluorescence mode using a Si(311) monochromator. The monochromator energy scale was calibrated using a Pd reference foil. All the spectra were collected by measuring simultaneously the Pd foil placed after the fluorescent detector *via* an ionization chamber. The data analysis was performed using the ATHENA and ARTEMIS software.[40] With ATHENA, the absorption edge, E_0, is determined, and the absorption due to the isolated atom is subtracted, by fitting the pre-edge and post-edge regions to obtain the EXAFS interference function, $\chi(k)$ and the normalized XANES spectra. The software ARTEMIS is used to perform the fit of the EXAFS region to scattering models in R-space obtained by FEFF, validated on the Pd foil. The amplitude reduction factor, S_0^2, was determined from the Pd foil best fit (0.88) and then kept fixed when fitting the data of all samples. The number of fitted parameters was always lower than the number of independent points.

Test to assess H-spillover

To check for the H-spillover, WO_3 was used to diagnose the activation of H_2 in the *catA-D* catalyst series, because the spilled-over H species migrates and readily reacts with the yellow WO_3 to form dark blue H_xWO_3.[41] Samples made with 1 g of WO_3 were mixed (or not) with 10 mg of catalyst and treated with H_2 (100 mL min⁻¹) at 25 °C for 2 min.

Catalytic hydrogenation of phenylacetylene in a batch reactor

Hydrogenation reactions were performed in a Top Industrie high-pressure and temperature stainless-steel autoclave with a controlling system. In a typical experiment, the autoclave was purged by three vacuum/argon cycles. A mixture containing the Pd catalyst (10 mg), 40 mL of a phenylacetylene solution in methanol (PhA/Pd ≈ 4000), and decane (75 mg, internal standard) was ultrasonicated for 5 min and then transferred into the autoclave under an Ar atmosphere. The autoclave was heated to 30 °C and pressurized with 5 bar of H_2; the stirring rate was fixed at 1000 rpm to avoid mass transfer limitations. The reaction test duration to reach 100% conversion was between 60 and 90 minutes, according to the catalyst in the *catA-D* series. Samples of the reaction mixture were taken periodically and then analyzed by GC-MS.

Catalytic hydrogenation of phenylacetylene in a continuous flow reactor

Three coated foams were inserted in a stainless steel milli-reactor (4.4 mm internal diameter, length of active zone of 75 mm) corresponding to an involved mass of 30 mg of Pd/CNT catalyst. Fluid delivery was ensured as a co-current up flow thanks to an HPLC pump (Shimadzu, LC2 0 AD) for the liquid and a mass-flow controller (Bronkhorst Elflow Prestige) for the gas. A simple T-junction upstream of the reactor ensures two fluid contacting. Temperature and pressure were controlled through a regulated electrical oven and a back-pressure regulator (Equilibar), respectively. Downstream, gas-liquid separation and liquid collection were made using a gravity-driven separator. In the experiments, H_2 gas flow rate was set to 20 N mL min⁻¹, and the liquid was set to the desired flow rate between 0.25 and 3.0 mL min⁻¹, corresponding to contact times between 0.4 and 5.1 s mol_{PhA}^{-1} mol_{Pd}^{-1}. The liquid

mixture consists of a solution of 0.16 M of PhA (Sigma Aldrich, 99%) in absolute ethanol (Sigma Aldrich) as solvent. A small amount of tetradecane (0.02 M) (Sigma Aldrich, 99%) has been used as an internal standard. Liquid phase analysis was made offline periodically thanks to GC-FID equipment (Shimadzu Nexis GC2030).

Computational details

Periodic Density Functional Theory (DFT) calculations were performed using the *ab initio* plane-wave pseudopotential approach, as implemented in the Vienna Ab initio Simulation Package (VASP; version 5.4).[42] The exchange–correlation potential was approximated with the generalized gradient approximation to the Perdew-Burke-Ernzerhof functional[43] and van der Waals interactions were taken into account through the D3 correction method of Grimme *et al*.[44] The core electrons were modeled using the Projector Augmented Wave (PAW) approach,[45] and the valence monoelectronic states were expanded using a plane wave basis set with a cutoff energy of 450 eV. Partial occupancies were estimated with a Gaussian smearing (σ) of 0.05 eV during all relaxations and extrapolating the energies to $\sigma = 0.00$ eV. As recently computationally modeled and described by some of us,[24a] the supported metal catalyst consists of an O-functionalized graphene (including experimentally probed abundant oxygen functional groups and point defects) as carbon support, together with a single Pd atom in a single vacancy and an ultra-small Pd_{13} nanoparticle as supported metal catalysts, the latter being hydrogenated with a ratio between adsorbed hydrides and surface metal atoms above unity. Γ-Centered ($3 \times 3 \times 1$) k-point mesh generated using the Monkhorst–Pack method was employed.[46] A vacuum region by at least 10 Å between the periodically repeated slabs was added to eliminate spurious interactions, and a dipole correction along the z-direction has been considered.[47] All structures were optimized until forces were less than 0.015 eV Å^{-1}. Transition states were first located using the Climbing Image version of the Nudged Elastic Band, CI-NEB, method,[48] and then properly optimized using the Quasi-Newton algorithm. Finally, they were proven to show a single imaginary frequency by the diagonalization of the numerical Hessian matrix with a step of 0.015 Å in both positive and negative directions of each coordinate.

References

[1]   S. A. Nikolaev, L. N. Zanaveskin, V. V. Smirnov, V. A. Averyanov, K. L. Zanaveskin, *Russian Chemical Reviews* **2009**, *78*, 231-247.

[2]   M. T. Ravanchi, S. Sahebdelfar, S. Komeili, *Reviews in Chemical Engineering* **2018**, *34*, 215-237.

[3]   C. Zhou, S. Yao, J. Wu, R. C. Forrey, L. Chen, A. Tachibana, H. Cheng, *Physical Chemistry Chemical Physics* **2008**, *10*, 5445-5451.

[4]   H. Okuyama, W. Siga, N. Takagi, M. Nishijima, T. Aruga, *Surface Science* **1998**, *401*, 344-354.

[5]   E. Wicke, H. Brodowsky, H. Züchner, in *Hydrogen in Metals II: Application-Oriented Properties* (Eds.: G. Alefeld, J. Völkl), Springer Berlin Heidelberg, Berlin, Heidelberg, **1978**, pp. 73-155.

[6]   J. A. Delgado, O. Benkirane, C. Claver, D. Curulla-Ferré, C. Godard, *Dalton Transactions* **2017**, *46*, 12381-12403.

[7]   J. A. Delgado, C. Godard, in *Recent Advances in Nanoparticle Catalysis* (Eds.: P. W. N. M. van Leeuwen, C. Claver), Springer International Publishing, Cham, **2020**, pp. 303-344.

[8]   R. G. Rao, R. Blume, T. W. Hansen, E. Fuentes, K. Dreyer, S. Moldovan, O. Ersen, D. D. Hibbitts, Y. J. Chabal, R. Schlögl, J.-P. Tessonnier, *Nature Communications* **2017**, *8*, 340.

[9]   S. F. Parker, H. C. Walker, S. K. Callear, E. Grünewald, T. Petzold, D. Wolf, K. Möbus, J. Adam, S. D. Wieland, M. Jiménez-Ruiz, P. W. Albers, *Chemical Science* **2019**, *10*, 480-489.

[10]   a) G. Carturan, G. Facchin, G. Cocco, S. Enzo, G. Navazio, *Journal of Catalysis* **1982**, *76*, 405-417; b) G. Del Angel, J. L. Benitez, *Reaction Kinetics and Catalysis Letters* **1993**, *51*, 547-553; c) G. Del Angel, J. L. Benitez, *Journal of Molecular Catalysis* **1994**, *94*, 409-416; d) D. Duca, L. F. Liotta, G. Deganello, *Journal of Catalysis* **1995**, *154*, 69-79; e) P. Weerachawanasak, O. Mekasuwandumrong, M. Arai, S.-I. Fujita, P. Praserthdam, J. Panpranot, *Journal of Catalysis* **2009**, *262*, 199-205; f) J. Hu, Z. Zhou, R. Zhang, L. Li, Z. Cheng, *Journal of Molecular Catalysis A: Chemical* **2014**, *381*, 61-69; g) P. V. Markov, I. S. Mashkovsky, G. O. Bragina, J. Wärnå, E. Y. Gerasimov, V. I. Bukhtiyarov, A. Y. Stakheev, D. Y. Murzin, *Chemical Engineering Journal* **2019**, *358*, 520-530.

[11]   Z. Xia, S. Zhang, F. Liu, Y. Ma, Y. Qu, C. Wu, *The Journal of Physical Chemistry C* **2019**, *123*, 2182-2188.

[12]   L. Xiang, H. Feng, M. Liu, X. Zhang, G. Fan, F. Li, *ACS Applied Nano Materials* **2021**, *4*, 4688-4698.

[13]   a) X.-P. Yin, S.-F. Tang, C. Zhang, H.-J. Wang, R. Si, X.-L. Lu, T.-B. Lu, *Journal of Materials Chemistry A* **2020**, *8*, 20925-20930; b) F. Yang, S. Ding, H. Song, N. Yan, *Science China Materials* **2020**, *63*, 982-992; c) C. Chen, W. Ou, K.-M. Yam, S. Xi, X. Zhao, S. Chen, J. Li, P. Lyu, L. Ma, Y. Du, W. Yu, H. Fang, C. Yao, X. Hai, H. Xu, M. J. Koh, S. J. Pennycook, J. Lu, M. Lin, C. Su, C. Zhang, J. Lu, *Advanced Materials* **2021**, *33*, 2008471; d) J. Wang, Q. Kuang, X. Su, X. Lu, L. Leng, M. Zhang, C. Guo, T. Li, Q. Xu, S. Sun, J. H. Horton, W. Wu, Z. Li, *ACS Applied Nano Materials* **2021**, *4*, 861-868; e) Z. Li, Q. Ren, X. Wang, W. Chen, L. Leng, M. Zhang, J. H. Horton, B. Liu, Q. Xu, W. Wu, J. Wang, *ACS Applied Materials & Interfaces* **2021**, *13*, 2530-2537.

[14]   E. Vorobyeva, E. Fako, Z. Chen, S. M. Collins, D. Johnstone, P. A. Midgley, R. Hauert, O. V. Safonova, G. Vilé, N. López, S. Mitchell, J. Pérez-Ramírez, *Angewandte Chemie International Edition* **2019**, *58*, 8724-8729.

[15]   C. Rivera-Cárcamo, I. C. Gerber, I. del Rosal, B. Guicheret, R. Castro Contreras, L. Vanoye, A. Favre-Réguillon, B. F. Machado, J. Audevard, C. de Bellefon, R. Philippe, P. Serp, *Catalysis Science & Technology* **2021**, *11*, 984-999.

[16]   I. C. Gerber, P. Serp, *Chemical Reviews* **2020**, *120*, 1250-1349.

[17]   U. Petek, F. Ruiz-Zepeda, M. Bele, M. Gaberšček, *Catalysts* **2019**, *9*, 134.

[18]   C. Rivera-Cárcamo, F. Leng, I. C. Gerber, I. del Rosal, R. Poteau, V. Collière, P. Lecante, D. Nechiyil, W. Bacsa, A. Corrias, M. R. Axet, P. Serp, *Catalysis Science & Technology* **2020**, *10*, 4673-4683.

[19]   C. Rivera-Cárcamo, C. Scarfiello, A. B. García, Y. Tison, H. Martinez, W. Baaziz, O. Ersen, C. Le Berre, P. Serp, *Advanced Materials Interfaces* **2021**, *8*, 2001777.

[20]   C.-T. Kuo, Y. Lu, L. Kovarik, M. Engelhard, A. M. Karim, *ACS Catalysis* **2019**, *9*, 11030-11041.

[21]   L. Zhang, K. Doyle-Davis, X. Sun, in *Supported Metal Single Atom Catalysis*, **2022**, pp. 169-198.

25

[22]   a) X. Chen, Y. Hou, H. Wang, Y. Cao, J. He, *The Journal of Physical Chemistry C* **2008**, *112*, 8172-8176; b) J. V. Rojas, C. H. Castano, *Radiation Physics and Chemistry* **2012**, *81*, 16-21; c) X. Xu, Y. Li, Y. Gong, P. Zhang, H. Li, Y. Wang, *Journal of the American Chemical Society* **2012**, *134*, 16987-16990; d) T. T. P. Cheung, *Surface Science* **1984**, *140*, 151-164.

[23]   a) W. Xiang, Y. Zhao, Z. Jiang, X. Li, H. Zhang, Y. Sun, Z. Ning, F. Du, P. Gao, J. Qian, K. Kato, M. Yamauchi, Y. Sun, *Journal of Materials Chemistry A* **2018**, *6*, 23366-23377; b) X. Huang, H. Yan, L. Huang, X. Zhang, Y. Lin, J. Li, Y. Xia, Y. Ma, Z. Sun, S. Wei, J. Lu, *The Journal of Physical Chemistry C* **2019**, *123*, 7922-7930.

[24]   a) J. Navarro-Ruiz, C. Rivera-Cárcamo, B. Machado, P. Serp, I. Del Rosal, I. C. Gerber, *ACS Applied Nano Materials* **2021**, *4*, 12235-12249; b) H. Yan, H. Cheng, H. Yi, Y. Lin, T. Yao, C. Wang, J. Li, S. Wei, J. Lu, *Journal of the American Chemical Society* **2015**, *137*, 10484-10487.

[25]   a) G. K. Wertheim, S. B. DiCenzo, D. N. E. Buchanan, *Physical Review B* **1986**, *33*, 5384-5390; b) A. Felten, J. Ghijsen, J. J. Pireaux, W. Drube, R. L. Johnson, D. Liang, M. Hecq, G. Van Tendeloo, C. Bittencourt, *Micron* **2009**, *40*, 74-79; c) M. Cini, M. De Crescenzi, F. Patella, N. Motta, M. Sastry, F. Rochet, R. Pasquali, A. Balzarotti, C. Verdozzi, *Physical Review B* **1990**, *41*, 5685-5695; d) I. Aruna, B. R. Mehta, L. K. Malhotra, S. M. Shivaprasad, *Journal of Applied Physics* **2008**, *104*, 064308.

[26]   C.-M. Lin, T.-L. Hung, Y.-H. Huang, K.-T. Wu, M.-T. Tang, C.-H. Lee, C. T. Chen, Y. Y. Chen, *Physical Review B* **2007**, *75*, 125426.

[27]   A. I. Frenkel, C. W. Hills, R. G. Nuzzo, *The Journal of Physical Chemistry B* **2001**, *105*, 12689-12703.

[28]   V. V. Srabionyan, A. L. Bugaev, V. V. Pryadchenko, L. A. Avakyan, J. A. van Bokhoven, L. A. Bugaev, *Journal of Physics and Chemistry of Solids* **2014**, *75*, 470-476.

[29]   K. Feng, H. Zhang, J. Gao, J. Xu, Y. Dong, Z. Kang, J. Zhong, *Applied Physics Letters* **2020**, *116*, 191903.

[30]   B. Gerand, M. Figlarz, in *Studies in Surface Science and Catalysis, Vol. 17* (Eds.: G. M. Pajonk, S. J. Teichner, J. E. Germain), Elsevier, **1983**, pp. 275-283.

[31]   S. Khoobiar, *The Journal of Physical Chemistry* **1964**, *68*, 411-412.

[32]   T. Katayama, T. Nitta, *Journal of Chemical & Engineering Data* **1976**, *21*, 194-196.

[33]   S. Zhao, J. Cai, H. Chen, J. Shen, *Catalysis Communications* **2021**, *157*, 106330.

[34]   a) I. T. Caga, E. Shutt, J. M. Winterbottom, *Journal of Catalysis* **1976**, *44*, 271-280; b) H. Song, Y. Liu, Y. Wang, B. Feng, X. Jin, T. Huang, M. Xiao, H. Gai, *Molecular Catalysis* **2020**, *493*, 111081; c) L. Ma, P. Jiang, K. Wang, K. Lan, X. Huang, M. Yang, L. Gong, Q. Jia, X. Mu, Y. Xiong, R. Li, *Journal of Alloys and Compounds* **2021**, *868*, 159047; d) L. Yang, L. Jin, X. Fang, Z. Cheng, Z. Zhou, *Industrial & Engineering Chemistry Research* **2017**, *56*, 14182-14191.

[35]   a) S. S. Han, H. Kim, N. Park, *The Journal of Physical Chemistry C* **2011**, *115*, 24696-24701; b) M. Tan, Y. Yang, Y. Yang, J. Chen, Z. Zhang, G. Fu, J. Lin, S. Wan, S. Wang, Y. Wang, *Nature Communications* **2022**, *13*, 1457.

[36]   a) R. C. Contreras, B. Guicheret, B. F. Machado, C. Rivera-Cárcamo, M. A. Curiel Alvarez, B. Valdez Salas, M. Ruttert, T. Placke, A. Favre Réguillon, L. Vanoye, C. de Bellefon, R. Philippe, P. Serp, *Journal of Catalysis* **2019**, *372*, 226-244; b) B. Guicheret, L. Vanoye, C. Rivera-Cárcamo, C. de Bellefon, P. Serp, R. Philippe, A. Favre-Réguillon, *ChemSusChem* **2022**, *15*, e202200916; c) L. Vanoye, B. Guicheret, C. Rivera-Cárcamo, R. Castro Contreras, C. de Bellefon, V. Meille, P. Serp, R. Philippe, A. Favre-Réguillon, *Chemical Engineering Journal* **2022**, *441*, 135951.

[37]   a) J. Yang, W. Li, D. Wang, Y. Li, *Small Structures* **2021**, *2*, 2000051; bX. Wu, H. Zhang, S. Zuo, J. Dong, Y. Li, J. Zhang, Y. Han, *Nano-Micro Letters* **2021**, *13*, 136.

[38]   F. Simescu-Lazar, T. Chaieb, S. Pallier, L. Veyre, R. Philippe, V. Meille, *Applied Catalysis A: General* **2015**, *508*, 45-51.

[39]   A. Borodziński, M. Bonarowska, *Langmuir* **1997**, *13*, 5613-5620.

[40]   B. Ravel, M. Newville, *Journal of Synchrotron Radiation* **2005**, *12*, 537-541.

[41]   Y. Xi, Q. Zhang, H. Cheng, *The Journal of Physical Chemistry C* **2014**, *118*, 494-501.

[42]   a) G. Kresse, J. Furthmüller, *Computational Materials Science* **1996**, *6*, 15-50; b) G. Kresse, J. Furthmüller, *Physical Review B* **1996**, *54*, 11169-11186.
[43]   J. P. Perdew, K. Burke, M. Ernzerhof, *Physical Review Letters* **1996**, *77*, 3865-3868.
[44]   S. Grimme, J. Antony, S. Ehrlich, H. Krieg, *The Journal of Chemical Physics* **2010**, *132*, 154104.
[45]   a) P. E. Blöchl, *Physical Review B* **1994**, *50*, 17953-17979; b) G. Kresse, D. Joubert, *Physical Review B* **1999**, *59*, 1758-1775.
[46]   H. J. Monkhorst, J. D. Pack, *Physical Review B* **1976**, *13*, 5188-5192.
[47]   G. Makov, M. C. Payne, *Physical Review B* **1995**, *51*, 4014-4022.
[48]   a) G. Henkelman, H. Jónsson, *The Journal of Chemical Physics* **2000**, *113*, 9978-9985; b) G. Henkelman, B. P. Uberuaga, H. Jónsson, *The Journal of Chemical Physics* **2000**, *113*, 9901-9904.

Table of Contents graphic
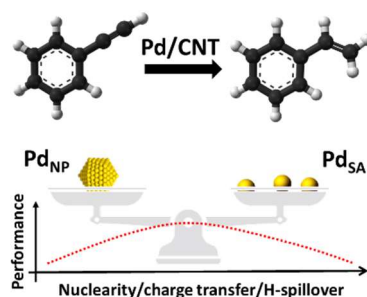
Selective hydrogenation: the performance of Pd/CNT catalysts for selective hydrogenation of phenylacetylene can be modulated by controlling the ratio between Pd nanoparticles and single atoms. DFT calculations suggest that the first coordination sphere of Pd single atoms has a pronounced effect on their reactivity.

28